



# Aerosol microphysical properties and CCN/INP information from lidar and ceilometer profiles: POLIPHON update

Albert Ansmann<sup>1</sup>, Julian Hofer<sup>1</sup>, Rodanthi-Elisavet Mamouri<sup>2,3</sup>, Moritz Haarig<sup>1</sup>, Holger Baars<sup>1</sup>, and Ulla Wandinger<sup>1</sup>

<sup>1</sup>Leibniz Institute for Tropospheric Research, Leipzig, Germany

<sup>2</sup>Eratosthenes Centre of Excellence, Limassol, Cyprus

<sup>3</sup>Cyprus University of Technology, Dep. of Civil Engineering and Geomatics, Limassol, Cyprus

**Correspondence:** A. Ansmann

(albert@tropos.de)

**Abstract.** Updated POLIPHON (Polarization Lidar Photometer Networking) conversion factors for the laser wavelengths of 355, 532, 911, and 1064 nm are presented. The conversion factors allow us to transfer profiles of aerosol-type-dependent optical properties measured with lidars and ceilometers into profiles of microphysical particle properties, and to estimate cloud condensation nucleus (CCN) and ice-nucleating particle (INP) concentrations at observed cloud levels. These updates were necessary to permit a coherent and harmonized data analysis of different long-term spaceborne lidar observations at 355 and 532 nm and to support ground-based lidar and ceilometer network measurements and research on aerosol-cloud interaction. The POLIPHON conversion factors are obtained by analyzing long-term sun photometer observations conducted at 60 AERONET (Aerosol Robotic Network) stations. Conversion factors are now available for mineral dust, marine aerosol, urban and rural anthropogenic particles, tropospheric and stratospheric wildfire smoke, and stratospheric volcanic sulfate aerosol.

## 10 1 Introduction

The POLIPHON (Polarization LIdar PHOtometer Networking) method (Ansmann et al., 2012; Mamouri and Ansmann, 2016, 2017) has been introduced 10–15 years ago to provide an easy-to-handle, robust, lidar-based option to estimate height profiles of particle mass (PM), cloud condensation nucleus (CCN) and ice-nucleating particle (INP) concentration from backscatter lidar profiles. Of key importance are look-up tables of aerosol-type-dependent conversion factors that are derived from global, long-term Aerosol Robotic Network (AERONET, Holben et al., 1998) sun photometer observations and that permit the conversion of particle optical into microphysical properties. The importance of such conversion tools arises from the fact that active remote sensing with lidars and ceilometers is the only way to monitor aerosol layers and embedded clouds in the atmospheres with high vertical resolutions and this continuously. Combined with cloud radar measurements, aerosol lidars provide the grounds for an observation-based in-depth investigation of aerosol-cloud interaction processes. In the framework of satellite-based lidar missions aerosols are characterized on a global scale. Long data sets, covering several decades are meanwhile collected with CALIOP (Cloud-Aerosol Lidar with Orthogonal Polarization, Winker et al., 2009, 2010) from 2006–2023, ALADIN (Atmospheric Laser Doppler Instrument, Baars et al., 2021; Trajon et al., 2025) from 2018–2023,

ADCL (Aerosol and Carbon dioxide Detection Lidar, Dai et al., 2024) since 2022, and ATLID (Atmospheric lidar, Wehr et al., 2023; Wandinger et al., 2023) since 2024.

25 The POLIPHON analysis scheme has been widely applied to analyze spaceborne and ground-based lidar observations of local, regional, and global pollution states, aerosol long-range-transport, and aerosol-cloud interaction (e.g., Ansmann et al., 2011, 2019a, 2025b; Córdoba-Jabonero et al., 2018; Baars et al., 2019; Haarig et al., 2019, 2025a; Hofer et al., 2020; Georgoulas et al., 2020; Jimenez et al., 2020, 2025; Engelmann et al., 2021; Radenz et al., 2021a; Floutsi et al., 2023; Mamouri et al., 2023; Janicka et al., 2023; Shang et al., 2024; Shen et al., 2024; Rogozovsky et al., 2025; Filioglou et al., 2025; Proestakis et al., 2025a, b; Malollari et al., 2025; He et al., 2025b). The broad spectrum of POLIPHON applications have been validated  
30 within a variety of field campaigns (e.g., Düsing et al., 2018; Mamali et al., 2018; Haarig et al., 2019; Marinou et al., 2019; Wieder et al., 2022; Choudhury et al., 2022). In this article, we present recent updates and new features of the POLIPHON method. The latest set of conversion factors based on the analysis of sun photometer observations at 60 AERONET sites around the globe is introduced as well.

35 The following facts and aspects motivated the updates: (1) The aerosol profiling community grew significantly. Besides operational ground-based lidar networks such as EARLINET (European Aerosol Research Lidar Network, Pappalardo et al., 2014) and the mentioned satellite lidar missions, dense ceilometer networks significantly contribute to aerosol profiling on continental scales (e.g., Cazorla et al., 2017; Flentje et al., 2021; Bellini et al., 2024). One of the main ceilometer laser wavelength is 910–911 nm. Consequently, conversion factors are needed that cover the entire laser wavelength spectrum used in active  
40 aerosol remote sensing. Therefore, conversion factors for 355, 532, 911, and 1064 nm are presented in this article.

(2) The launch of ATLID (laser wavelength of 355 nm) aboard the EarthCARE (Earth Cloud Aerosol and Radiation Explorer, Wehr et al., 2023) satellite in May 2024 prompted us to carefully reevaluate the 355 nm conversion factors, now for five basic aerosol types considered in the POLIPHON look-up tables. Furthermore, to obtain coherent, harmonized time series of global aerosol data sets since the start of the CALIOP satellite lidar, operated at 532 nm, we need updated POLIPHON conversion  
45 factor pairs for 355 and 532 nm to combine the CALIOP long-term observations with the EarthCARE measurements and to include even additional long-term observations with ALADIN and the ACDL.

(3) The study of Kulkarni et al. (2025) motivated us to improve the statistical analysis applied to obtain the POLIPHON conversion factors. These authors found that our parameterization scheme applied to estimate the CCN concentration  $n_{CCN}$  from the observed particle extinction coefficient  $\sigma$  does not work well and overestimates the CCN concentration in the case  
50 of continental aerosol pollution. In our original statistical approach (Mamouri and Ansmann, 2016), we followed the recommendation of Shinozuka et al. (2015) and derived the respective extinction-to-CCN conversion factor from a linear correlation between  $\log(\sigma)$  and  $\log(n_{50})$  data, with  $n_{50}$  considering all particles with dry-particle radius  $>50$  nm and used as proxy for  $n_{CCN}$ . Obviously, our statistical correlation analysis failed caused by too noisy  $n_{50}$  data and the impact of outliers, with the consequence that the derived extinction-to-CCN conversion factors were too large. In this study, we apply a weighted linear  
55 regression analysis to  $\sigma$  and  $n_{50}$  data fields in linear scales (York et al., 2004). This approach is better in line with alternative retrieval schemes of Choudhury and Tesche (2022) and Lenhardt et al. (2023) and, most important, efficiently removes unwanted outliers.



The paper is organized as follows. In Sect. 2, we briefly explain the POLIPHON method and highlight the changes and improvements compared to the version presented in Mamouri and Ansmann (2016, 2017) and Ansmann et al. (2019b, 2021). In Sect. 3, we introduce the downloaded AERONET data of spectral aerosol optical thicknesses (AOTs) and size distributions and all the AERONET stations we considered in this POLIPHON-update project. We significantly increased the number of AERONET stations involved in the correlation studies to obtain the conversion factors. Even several Arctic and Antarctic AERONET stations are included to derive conversion factors for stratospheric wildfire smoke and volcanic sulfate layers. In Sect. 3.4, we discuss in detail how we handle observations performed at ambient humidity conditions to obtain conversion factors for dry aerosol particles, as requested by the atmospheric modeling community. Number, surface area, and volume concentrations of dry particles are required as input in CCN and INP parameterization schemes. In Sect. 4, all conversion factors for all defined 5 different aerosol types are presented and discussed. A brief conclusion section is given in Sect. 5. The statistical analysis (least-squares estimation (LSE) method) applied to the AERONET observations of optical and microphysical properties is described in Appendix A.

## 2 POLIPHON method: A compact overview

In this section, we provide a brief overview of the POLIPHON method. More details can be found in Mamouri and Ansmann (2014, 2016, 2017). A detailed description of the POLIPHON technique with focus on dust properties is given in Marinou et al. (2019), Ansmann et al. (2019b), and He et al. (2023, 2025a) as well. An extension towards wildfire smoke retrieval was discussed in Ansmann et al. (2021). The principle idea, concept, and data analysis scheme of the POLIPHON is illustrated in Fig. 1. The aerosol types considered in the updated POLIPHON data analysis are listed in Table 1.

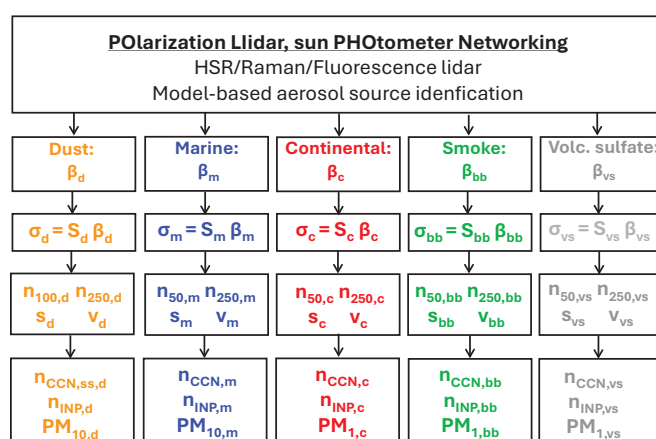


**Figure 1.** The POLIPHON approach to derive microphysical and cloud-process-relevant aerosol properties of five aerosol types (listed in the 4th and 5th row) from lidar observations of optical properties (backscatter and extinction coefficients  $\beta_i$  and  $\sigma_i$ , respectively, linked by the extinction-to-backscatter ratio  $S_i$ ). In the identification of the aerosol types, aerosol transport modeling is used as well. The different data analysis steps and listed aerosol parameters are explained in the following subsections 2.1 to 2.5.



**Table 1.** Aerosol types considered in the determination of updated POLIPHON conversion factors. Besides the main aerosol types, marine aerosol, mineral dust with fine-mode (df) and coarse-mode (dc) fraction, and continental anthropogenic haze, we consider biomass burning (bb) smoke (in the lower troposphere and the UTLS) and stratospheric volcanic sulfate (vs) in the respective regression analysis applied to obtain the conversion factors.

Aerosol type	Index $i$
Continental haze	c
Marine aerosol	m
Mineral dust	d, df, dc
Biomass burning smoke	bb
Volcanic sulfate	vs

## 2.1 Step 1: Separation of dust and non-dust optical properties

The POLIPHON data analysis consists of five steps. An overview of the main retrieval packages is shown in Table 2. In the first step, the dust and non-dust contributions to the particle backscatter coefficient are separated by using the measured profile of the particle linear depolarization ratio (Tesche et al., 2009; Mamouri and Ansmann, 2014). However, this is only possible if a polarization-sensitive lidar or ceilometer is operated. Besides non-spherical dust particles, volcanic ash, wildfire smoke in the upper troposphere and lower stratosphere (UTLS) and dry marine particles in the shallow marine boundary layer can cause enhanced light depolarization (Ansmann et al., 2010; Haarig et al., 2017, 2018). However, by using backward trajectory analysis these contributions to the measured depolarization ratio can be easily identified so that a clear quantification of the dust backscatter coefficient is possible. Step 1 is important because mineral dust belongs to the key aerosol types in the atmosphere and influences cloud processes in a very specific way as will be discussed below. If a polarization-sensitive lidar instrument is not available, one may use available modeled aerosol profile information to estimate the dust backscatter fraction, as described in the next section.

## 2.2 Step 2: Identification of the aerosol types

Aerosol-type and aerosol source information for detected aerosol layers can be generally obtained, e.g., via height-resolved air mass source attribution (Radenz et al., 2021b), backward trajectory analysis (Stein et al., 2015), or from large-scale atmospheric simulations with the CAMS (Copernicus Atmosphere Monitoring Service) model. CAMS is a global atmospheric composition forecast production system (Amarillo et al., 2024). Furthermore, simultaneously measured extinction and backscatter profiles observed with Raman lidar or High Spectral Resolution Lidar (HSRL) can be used to identify the non-dust aerosol types in the observed layers (Giannakaki et al., 2020) when using a polarization lidar.

Complex mixtures of aerosols, as they may frequently occur in coastal polluted areas near deserts as for example in the Eastern Mediterranean (Rogozovsky et al., 2025), are probably the most difficult scenarios regarding a proper identification



**Table 2.** Overview of the computations and conversions within the POLIPHON data analysis. The primary retrieval products ( $n_{50,i,\text{dry}}$  to  $n_{250,i,\text{dry}}$ ,  $s_{i,\text{dry}}$ ,  $v_{i,\text{dry}}$ ) for dry aerosol conditions are calculated from aerosol-type-dependent particle extinction coefficients  $\sigma_{i,\text{amb}}(\lambda)$  observed at ambient conditions (index: amb) and laser wavelength  $\lambda$ .  $r$  denotes particle radius. The dry-aerosol products are requested input data in the particle mass estimation and CCN and INP parameterizations (products for environmental and cloud studies). Details to CCN estimations and the different ice nucleation modes (IF, ABIFM, DIN, HOM) as well as the relevant literature for the respective parameterizations (D10, D15, U17, KA13, W12, K00) are given in the text. The units (column 3) are given for the products ( $\beta$ ,  $\sigma$ ,  $n$ ,  $s$ ,  $v$ ,  $M$ ,  $n_{\text{CCN}}$ ,  $n_{\text{INP}}$ ).

Parameter	Product/computation	Unit
<b>Lidar observation</b>		
Particle backscatter coefficient	$\beta_{i=\text{d,amb}}(\lambda), \beta_{i\neq\text{d,amb}}(\lambda)$	$\text{Mm}^{-1} \text{sr}^{-1}$
Particle extinction coefficient	$\sigma_{i,\text{amb}}(\lambda) = S_{i,\text{amb}}(\lambda) \beta_{i,\text{amb}}(\lambda)$	$\text{Mm}^{-1}$
<b>Primary retrieval products</b>		
Part. number conc. ( $r > 50 \text{ nm}$ )	$n_{50,i,\text{dry}} = c_{50,i}(\lambda) \sigma_{i,\text{amb}}(\lambda)$	$\text{cm}^{-3}$
Part. number conc. ( $r > 100 \text{ nm}$ )	$n_{100,i,\text{dry}} = c_{100,i}(\lambda) \sigma_{i,\text{amb}}(\lambda)$	$\text{cm}^{-3}$
Part. number conc. ( $r > 250 \text{ nm}$ )	$n_{250,i,\text{dry}} = c_{250,i}(\lambda) \sigma_{i,\text{amb}}(\lambda)$	$\text{cm}^{-3}$
Particle surface concentration	$s_{i,\text{dry}} = c_{s,i}(\lambda) \sigma_{i,\text{amb}}(\lambda)$	$\mu\text{m} \mu\text{m}^2 \text{cm}^{-3}$
Particle volume concentration	$v_{i,\text{dry}} = c_{v,i}(\lambda) \sigma_{i,\text{amb}}(\lambda)$	$\mu\text{m}^3 \text{m}^{-3}$
<b>Products for environmental and cloud studies</b>		
Particle mass concentration	$M_{i,\text{dry}} = \rho_i v_{i,\text{dry}}$	$\mu\text{g m}^{-3}$
CCN concentration ( $i=\text{c,m,bb}$ )	$n_{\text{CCN},0.2\%,i} = n_{50,i,\text{dry}}$	$\text{cm}^{-3}$
CCN concentration ( $i=\text{d}$ )	$n_{\text{CCN},0.2\%,\text{d}} = n_{100,\text{d,dry}}$	$\text{cm}^{-3}$
INP conc., time-indep., $i=\text{d}$	$n_{\text{INP},\text{d}}$ (D15,IF, $n_{250,\text{d,dry}}$ )	$\text{L}^{-1}$
INP conc., time-indep., $i=\text{c}$	$n_{\text{INP},\text{c}}$ (D10,IF, $n_{250,\text{c,dry}}$ )	$\text{L}^{-1}$
INP conc., time-indep., $i=\text{d}$	$n_{\text{INP},\text{d}}$ (U17,DIN, $s_{\text{d,dry}}$ )	$\text{L}^{-1}$
INP conc., time-dep. ( $i=\text{d,bb}$ )	$n_{\text{INP},i}$ (KA13,ABIFM, $s_{i,\text{dry}}$ )	$\text{L}^{-1}$
INP conc., time-dep. ( $i=\text{d,bb}$ )	$n_{\text{INP},i}$ (W12,DIN, $s_{i,\text{dry}}$ )	$\text{L}^{-1}$
INP conc., time-dep. ( $i=\text{vs}$ )	$n_{\text{INP},\text{vs}}$ (K00,HOM, $u_{\text{vs,dry}}$ )	$\text{L}^{-1}$

of all contributing aerosol types. However, in the majority of aerosol scenarios, the aerosol conditions are much more simple, as numerous lidar observations of well-defined lofted desert dust plumes, pronounced wildfire smoke layers, marine aerosols over the remote oceans, or of the anthropogenically polluted boundary layer over the industrial continents show.

100 Note that conversion factors for volcanic ash are not included in Table 1. The volcanic ash conversion factors are very similar to the ones for mineral dust as observations showed (Ansmann et al., 2011).



### 2.3 Step 3: Conversion of aerosol-type-dependent backscatter into extinction coefficients

In the third step, the aerosol-type-dependent components  $\beta_i(\lambda)$  of the observed particle backscatter coefficient must be converted into respective particle extinction coefficients  $\sigma_i(\lambda)$  by using published data sets of aerosol-type-dependent extinction-to-backscatter ratios or lidar ratios  $S_i(\lambda)$  (Müller et al., 2007; Groß et al., 2013; Haarig et al., 2018, 2025b; Floutsi et al., 2023, 2024). Meanwhile, many publications for lidar ratios at  $\lambda = 355$  nm and 532 nm, and a few reports for the wavelength of 1064 nm are available in the literature (Haarig et al., 2022, 2025b). The new generation of space lidars (355 and 532 nm HSRLs), measuring both the backscatter and the extinction coefficient of a given aerosol mixture, is able to produce its own aerosol-type-dependent lidar-ratio climatology by analyzing the observations, e.g., in pure dust or pure marine regions, in dense wildfire smoke plumes (Haarig et al., 2025a), or highly polluted urban areas.

### 2.4 Step 4: Conversion of aerosol-type-dependent extinction coefficients into microphysical properties

In the fourth step, the POLIPHON extinction-to-number conversion factors  $c_{50,i}(\lambda)$ ,  $c_{100,i}(\lambda)$ , and  $c_{250,i}(\lambda)$ , the extinction-to-surface-area conversion factors  $c_{s,i}(\lambda)$ , and the extinction-to-volume conversion factors  $c_{v,i}(\lambda)$  are applied to convert the lidar-derived aerosol-type-dependent extinction coefficients  $\sigma_i(\lambda)$  into particle number concentration  $n_{50,i}$  (considering all particles with dry-particle radius  $>50$  nm),  $n_{100,i}$  (considering all particles with dry-particle radius  $>100$  nm), and  $n_{250,i}$  (considering all particles with dry-particle radius  $>250$  nm), and into surface area ( $s_i$ ) and volume concentrations ( $v_i$ ). Table 2 (primary retrieval products) provides an overview of these conversions. The dry-aerosol products (index: dry) are required as input in the estimation of particle mass, CCN, and INP concentrations. The dry-aerosol properties are, however, derived from extinction coefficients  $\sigma_{i,amb}(\lambda)$  measured at ambient humidity conditions (Index: amb). The impact of water uptake by aerosol particles is small and thus the uncertainty introduced by unknown water uptake effects as long as the relative humidity (RH) is  $<70\%$ . Aerosol particles can be regarded as dry at  $RH < 50\%$ . At  $RH > 75\%$  significant water uptake occurs in the case of hygroscopic particles such as anthropogenic sulfate particles (Skupin et al., 2016). The water-uptake impact must be considered in the POLIPHON data analysis. This aspect is further discussed in Sect. 3.4.

According to Table 2, the conversion factors are designed in such a way that the required dry-particle microphysical products can be directly obtained from the observations (conducted at ambient conditions). Besides the number, surface, and volume concentrations in Table 2 further products are computed in the case of dust, such as  $n_{60,d,dry}$ ,  $s_{100,d,dry}$ ,  $v_{dc,dry}$ , and  $v_{df,dry}$ . The quantities will be explained in Sect. 3.1.

### 2.5 Step 5: Estimation of mass concentrations and cloud-relevant products

In the fifth and final step of the POLIPHON data analysis, the aerosol products, which are of importance for environmental monitoring and studies of aerosol-cloud interaction, are calculated. The dry-particle mass concentration  $M_{i,dry}$  is obtained from the derived volume concentration  $v_{i,dry}$  in combination with particles density information. The particle densities  $\rho_d$ ,  $\rho_c$ ,  $\rho_m$ , and  $\rho_{bb}$  for dust, continental aerosol pollution, dry marine particles, and wildfire smoke particles are set to  $2.6 \text{ g cm}^{-3}$ ,  $1.5 \text{ g cm}^{-3}$ ,  $2.16 \text{ g cm}^{-3}$ , and  $1.15 \text{ g cm}^{-3}$ , respectively (Ansmann et al., 2012, 2021). The particle density for stratospheric



sulfate particles  $\rho_{vs}$  is a strong function of temperature (Wandinger et al., 1995). The  $H_2SO_4$  concentration of the sulfuric  
135 acid-water solution droplets can be calculated by using model-based temperatures and by assuming a typical water vapor  
concentrations, e.g. of 5 ppm in the dry lower stratosphere.

An important POLIPHON application is the estimation of CCN and INP concentrations in the vertical profile up to tropopause  
level. Dust particles play a special role in aerosol-cloud-interaction processes. They are omnipresent in the atmosphere (Froyd  
et al., 2022). On the one-hand side, pure dust particles are hydrophobic in contrast to other relevant aerosol types, such as  
140 marine or anthropogenic pollution particles. Thus, dust particles seem to be quite inefficient CCN (Kumar et al., 2009; Koehler  
et al., 2009) as long as they are not internally mixed with soluble, hygroscopic material. On the other-hand side, mineral dust  
is the most important INP type (DeMott et al., 2015; Kanji et al., 2017). The number concentrations  $n_{50,i,dry}$  and  $n_{100,d,dry}$   
in Table 2 (primary POLIPHON products) are used as CCN proxies  $n_{CCN,0.2\%,i}$  for hygroscopic ( $i=c,m,bb$ ) and hydrophobic  
(dust,  $i=d$ ) particles, respectively, for a typical water supersaturation ratio of 0.2% (relative humidity over water of 100.2%).  
145 Such a supersaturation is reached during updraft conditions with low vertical velocities of clearly below 1 m/s. At stronger  
updraft speeds and correspondingly higher supersaturation values of 0.4 to 0.7%, the  $n_{CCN}$  values may be a factor of 5–10  
higher than the ones for 0.2% as we pointed out in (Mamouri and Ansmann, 2016).

Two different INP parameterization concepts are discussed in the literature and used in simulation models, the time-  
independent (diagnostic) approach and the time-dependent (prognostic) approach (Knopf et al., 2023). The time-independent  
150 approach includes a time-independent particle-number- and surface-area-based descriptions of ice nucleation (DeMott et al.,  
2010, 2015; Ullrich et al., 2017), denoted as D10, D15, and U17, respectively, in Table 2. The particle number concentration  
 $n_{250,c,dry}$  (considering continental, insoluble particles with radius  $>250$  nm) is used as aerosol input in the D10,IF parame-  
terization scheme to estimate the INP concentration in the case of immersion freezing (IF). Immersion freezing means that  
nucleation occurs on an insoluble particle which is immersed in a cloud water droplet (DeMott et al., 2010). The dust particle  
155 number concentration  $n_{250,d,dry}$  is used as aerosol input in the D15,IF parameterization scheme used to estimate the dust INP  
concentration (DeMott et al., 2015). Ullrich et al. (2017) provides a deposition ice nucleation (DIN) parameterization for dust  
particles. DIN (ice nucleation initiated by water vapor deposition on INPs) typically occurs at cirrus level and temperatures  
 $< -40^\circ C$ . The dust surface area concentration  $s_{d,dry}$  is the aerosol input. Further diagnostic INP parameterization for marine  
particles (McCluskey et al., 2018), biological aerosol components (Tobo et al., 2013), and organic particles (Tobo et al., 2014)  
160 are available, but not listed in Table 2. Aerosol input is always the surface area concentration.

The time-dependent approach to immersion freezing is following the classical nucleation theory (CNT) (Pruppacher and  
Klett, 1997; Knopf and Alpert, 2013; Alpert and Knopf, 2016; Knopf et al., 2023). In the time-dependent approach, all particles  
can be activated at a random base and belong to the reservoir of INPs within a given cloud layer. Aerosol-type-dependent  
nucleation rates control the nucleation of ice crystals per second (Knopf et al., 2023). According to DeMott et al. (2010, 2015)  
165 and Schneider et al. (2025) the large particles with radius  $>250$  nm are the most favorable INPs. We may thus introduce the  
number concentration  $n_{250,i,dry}$  as INP reservoir proxy. In Knopf and Alpert (2013) (KA13, ABIFM: water-activity based  
immersion freezing model) and Wang et al. (2012) (W12, DIN), time-dependent INP parameterizations for immersion freezing  
and deposition ice nucleation, respectively are described.



170 Finally, an INP parameterization for homogeneous freezing is listed (Koop et al., 2000) (K00, HOM). This ice nucleation mode describes freezing of liquid sulfate particles (background aerosol particles or volcanic sulfate particles in the upper troposphere) at temperatures below  $-40^{\circ}\text{C}$ . Here, the volume concentration  $v_{\text{vs}}$  is the aerosol input parameter. Note, that all ice nucleation processes are strong functions of temperature, relative humidity, and vertical wind conditions (creating the ice supersaturation conditions required to start ice crystal nucleation). More discussion on INP retrieval and estimation with focus on lidar INP profiling are given in Mamouri and Ansmann (2016) and Ansmann et al. (2019b, 2021, 2023, 2025a).

### 175 3 POLIPHON conversion factors from AERONET observations

#### 3.1 Data analysis concept

Main goal of the article is to present an updated set of POLIPHON conversion factors  $c_{50,i}(\lambda)$ ,  $c_{100,i}(\lambda)$ ,  $c_{250,i}(\lambda)$ ,  $c_{s,i}(\lambda)$ , and  $c_{v,i}(\lambda)$  for five different aerosol types, defined in Table 1, and four lidar/ceilometer laser wavelengths. The POLIPHON conversion factors required in Table 2 are obtained from statistical analyses (explained in the Appendix A) of the correlation  
180 between two data records  $x_{i,j}(\lambda)$  and  $y_{i,j}$ . The data set  $x_{i,j}(\lambda)$  contains all individual observations (from  $j = 1$  to  $N_{\text{obs}}$ ) of the aerosol optical thickness  $\text{AOT}_{i,j}$  for wavelength  $\lambda$  and aerosol type  $i$  measured at one of the selected AERONET sites. The data set  $y_{i,j}$  contains the column-integrated values of one of the microphysical retrieval products such as  $\int n_{50,i,j}(z)dz$ ,  $\int n_{250,i,j}(z)dz$ ,  $\int s_{i,j}(z)dz$ , or  $\int v_{i,j}(z)dz$  with height  $z$  above the AERONET station.

The AERONET data base stores all individual observations of the AOT from 340 to 1640 nm and the related column-  
185 integrated particle size distribution for all AERONET sites. The size distributions are obtained by applying a well-designed and validated comprehensive inversion scheme (Dubovik and King, 2000; Dubovik et al., 2000, 2006) to the spectrally resolved AOT observations and the measured spectral sky radiances. From the particle size distributions, the column-integrated properties  $\int n_{50,i}(z)dz$ ,  $\int n_{250,i}(z)dz$ ,  $\int s_i(z)dz$ , and  $\int v_i(z)dz$ , are calculated in the first step of the data analysis to obtain the POLIPHON conversion factors. Details are given in Mamouri and Ansmann (2016, 2017). As will be presented in the next  
190 section, we selected preferably AERONET sites with long-term observation over more than 10 years and thus having data records of the order 1000–100000 individual observations of optical and corresponding microphysical properties.

In the next step, a linear regression study is applied for a well-defined subgroup of AERONET observations, e.g., for all dust-dominated observations (aerosol type index  $i = \text{d}$ ) collected at a given near-desert station. The statistical analysis is repeated for all selected AERONET stations within or close to a desert. The applied least-squares estimation (LSE) method (York  
195 et al., 2004), described in the Appendix A, considers all individual dust observational data sets  $\text{AOT}_{i,j}(\lambda)$ ,  $\int n_{100,d,j}(z)dz$ ,  $\int n_{250,d,j}(z)dz$ ,  $\int s_{d,j}(z)dz$ , and  $\int v_{d,j}(z)dz$ , collected at one station. For each data set consisting of pairs of a given  $\text{AOT}_{i,j}(\lambda)$  and one of the defined microphysical products, e.g., of the dust particle volume concentration  $v_{d,j}$ , the linear regression analysis is performed and yields the conversion factor, e.g., the dust extinction-to-volume conversion factor  $c_{v,d}(\lambda)$  as needed in Table 2. For dust, the linear regression analysis is performed with 8 different microphysical properties ( $\int n_{60,d,j}(z)dz$ ,  
200  $\int n_{100,d,j}(z)dz$ ,  $\int n_{250,d,j}(z)dz$ ,  $\int s_{d,j}(z)dz$ ,  $\int s_{100,d,j}(z)dz$ ,  $\int v_{d,j}(z)dz$ ,  $\int v_{\text{df},j}(z)dz$ , and  $\int v_{\text{dc},j}(z)dz$ ). In all other cases (marine and continental aerosol, wildfire smoke, and volcanic stratospheric sulfate), four regression studies are conducted



per wavelength with  $AOT_{i,j}(\lambda)$  and with one of the four defined microphysical products  $\int n_{50,i,j}(z)dz$ ,  $\int n_{250,i,j}(z)dz$ ,  $\int s_{i,j}(z)dz$ , and  $\int v_{i,j}(z)dz$ .

The long list of 8 dust conversion factors is related to specific role of dust in cloud processes. Freshly emitted hydrophobic dust particles may be rather inefficient CCN. Only particles with radius  $>100 \mu\text{m}$  or even larger ones, partly  $>200 \mu\text{m}$  in radius, may be able to serve as CCN. However, dust particles coated with hygroscopic substances may act as CCN already at radius sizes of  $>50\text{-}60 \mu\text{m}$ . With  $n_{60,d,dry}$ , we introduce a new CCN proxy for contaminated dust, e.g., dust particles with sulfate coating.

In the case of ice nucleation, the surface area concentration  $s_d$  is usually the input parameter in INP parameterization. However, in immersion freezing processes with hydrophobic dust INPs, only the surface area concentration of the activated CCN ( $n_{100,d}$ ) inside the droplets is then relevant in heterogeneous ice nucleation processes, i.e., the surface area  $s_{100,d}$  considering only the dust particles with radius  $>100 \text{ nm}$  should be used as aerosol input parameter in the INP parameterizations.

For a number of reasons summarized by Proestakis et al. (2025a, b), especially when illuminating the life cycle of dust in the atmosphere, lidar-derived profiles of fine-mode and coarse-mode dust mass concentrations are useful to improve parameterizations of dust emission, long-range transport and deposition in atmospheric models. Lidar-model comparisons regarding fine-mode and coarse-mode fractions during long-range transport were discussed in Ansmann et al. (2017). Therefore, we include extinction-to-volume conversion factors for fine mode  $c_{v,df}$  and coarse mode  $c_{v,dc}$ .

For a given station (assigned to one of the five aerosol types), the regression analysis is repeated for each of the different 4–8 microphysical products to obtain the respective set of 4–8 conversion factors. This procedure is repeated for each of the four wavelengths. In the final step, we averaged all station-by-station conversion factors (for a given aerosol type, wavelength, and microphysical product) to obtain the mean conversion factors for all defined aerosol types and wavelengths. In the next two sections, we introduce the selected 60 AERONET stations and how we filtered the AERONET data sets to obtain the aerosol-type-dependent AERONET data sets required as input in the regression analyses.

### 3.2 Selected AERONET stations

Table 3 and Fig. 2 provide an overview of all selected 60 AERONET stations used in our statistical data analysis. We selected 12 AERONET stations in or close to desert regions to be able to determine conversion factors for pure desert dust conditions ( $i=d$ ). Similarly, we selected 8 stations on islands in the Pacific, Indian, and Atlantic Ocean with long-term observations of more than 10 years in order to derive representative marine-aerosol conversion factors ( $i=m$ ). In the case of continental anthropogenic pollution ( $i=c$ ), we selected 25 AERONET stations to cover remote (background), rural, and urban conditions on different continents.

In the case of wildfire smoke observations ( $i=bb$ ), we used the stations, data sets, and data filtering options in this POLIPHON update effort as selected in Ansmann et al. (2021). However, this time, we excluded the observations at the Table Mountain station in California. The impact of urban haze from the Los Angeles region is always high and does not allow a trustworthy retrieval of pure smoke conversion factors. In Ansmann et al. (2021), conversion factors for 532 nm were presented, only. Now



**Table 3.** Overview of AERONET stations, selected to obtain the conversion factors for mineral dust, marine aerosol, continental haze, biomass burning smoke, and volcanic sulfate aerosol in the stratosphere.

AERONET site	Acronym	AERONET site	Acronym	AERONET site	Acronym
<u>Mineral dust (<math>i = d</math>)</u>		<u>Continental haze (<math>i = c</math>)</u>		<u>Biomass burning smoke (<math>i = bb</math>)</u>	
Tamanrasset, Algeria	TAM	G. Dahlen Lighth., Sweden	GDL	Reno, USA	REN
Sal, Cabo Verde	SAL	Kuopio, Finland	KUO	Mongu, Zambia	MON
Izaña, Tenerife, Spain	IZA	Watnall, United Kingdom	WAT	Mukdahan, Thailand	MUK
Ragged Point, Barbados	RAG	Moscow, Russia	MOS	Singapore, Singapore	SIN
Sede Boker, Israel	SED	Leipzig, Germany	LEI	Alta Floresta, Brazil	ALT
Solar Village, Saudi Arabia	SOL	Lille, France	LIL	Yellowknife, Canada	YEL
Dushanbe, Tajikistan	DUS	Davos, Switzerland	DAV	Churchill, Canada	CHU
Lanzhou(SACOL), China	LZH	Modena, Italy	MOD	CEILAP-RG, Argentina	CEI
White Sands, USA	WHI	Valladoloid, Spain	VAL	Punta Arenas, Chile	PUN
Trelew, Argentina	TRE	Athens, Greece	ATH	Marambio, Arg. Antarctica	MAR
Birdsville, Australia	BIR	Tel Aviv (Weizmann), Israel	TEL		
Gobabeb, Namibia	GOB	Cairo, Egypt	CAI	<u>Volcanic sulfate (<math>i = vs</math>)</u>	
		Beijing, China	BEI	Windpoort, Namibia	WIN
		Pokhara, India	POK	Gobabeb, Namibia	GOB
<u>Marine aerosol (<math>i = m</math>)</u>				Metsi, South Africa	MET
Ragged Point, Barbados	RAG	Chiba, Japan	CHI	Maïdo, La Reunion, France	MAI
Lanai, Hawaii, USA	LAN	Yakutsk, Russia	YAK	SP-Each, Brazil	SPE
Graciosa, Azores, Portugal	GRA	Bangkok, Thailand	BAN	PSDA, Chile	PSD
Nauru, Nauru	NAU	Mbita, Kenya	MBI	Utsteinen, Antarctica	UTS
Tahiti, Tahiti	TAH	Pretoria, South Africa	PRE		
Midway Island, Pacific	MID	Greenbelt (GSFC), USA	GRE		
Pago Pago, Amer. Samoa	PAG	Southern Great Plains, USA	SGP		
Amsterdam Island, Pacific	AMS	Los Angeles (Caltech), USA	LOS		
		Bonanza Creek, USA	BON		
		São Paulo, Brazil	SAO		
		Canberra, Australia	CAN		

235 we repeated all computations for all four wavelengths including 355, 911, and 1064 nm, and applied, for the first time, also a weighted linear regressions analysis (York et al., 2004) to the wildfire smoke observations.

In the case of the stratospheric sulfate conversion factors for fresh volcanic aerosol (from the Hunga Tonga-Hunga Ha'apai volcanic eruption in mid-January 2022, in the following simply denoted as Hunga Tonga eruption), we used the same observations (stations, measurement days, observation times) as presented in Figs. 3 and 4 in Boichu et al. (2023). These stations are

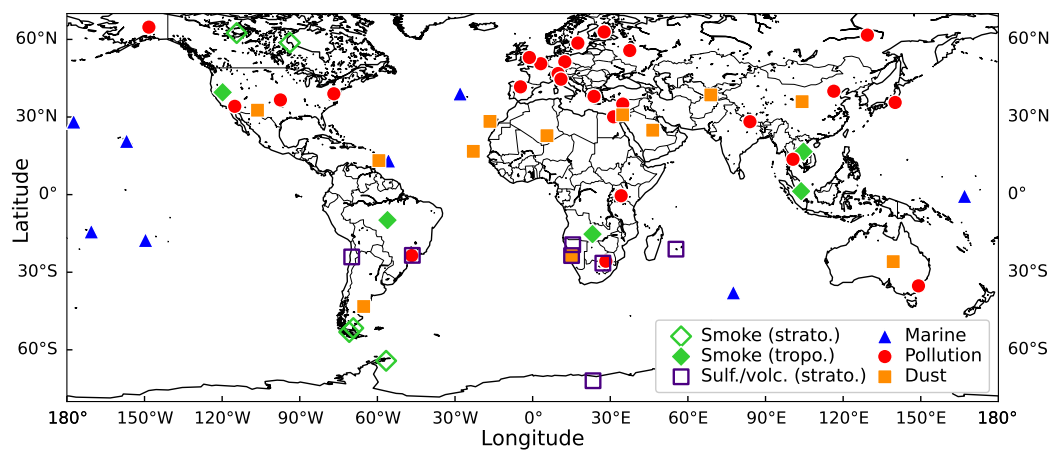


**Figure 2.** Distribution of the selected 60 AERONET stations over the globe. For the determination of marine, continental (urban, rural), and dust conversion factors, we used the observations at 8 marine AERONET stations (blue triangles), at 25 continental sites (red circles), at 12 stations close to deserts (orange squares). Observations of strong wildfire smoke events at 10 stations (green and white diamonds) and of pronounced volcanic sulfate layers at 7 sites (open squares) allowed the retrieval of wildfire smoke and volcanic sulfate conversion factors.

240 Maïdo on La Reunion, France, Windpoort and Gobabeb in Namibia, Metsi in South Africa, SP-EACH at São Paulo, Brazil, and PSDA, Chile, located in the Antofagasta region in northern Chile. The observations in late-January 2022 are characteristic for fresh sulfate (effective radius around 300 to 500 nm) with a low impact of sedimentation and removal of large particles. The volcanic sulfate particles formed a well defined accumulation mode (similar to the one of UTLS wildfire smoke).

To obtain conversion factors for aged Hunga Tonga sulfate aerosol, one year after the eruption, we used the observations at  
245 the Antarctic AERONET site of Utsteinen (23.3°E, 72°S, 1400 m above sea level, 160 km away from the Southern Ocean). The 500 nm AOT is close to 0.02 at unperturbed atmospheric conditions over the Antarctic stations so that any further AOT contribution, e.g., from the stratosphere, is visible in the data. The effective radius was 160 nm for these unperturbed aerosol conditions in January 2022. One year later, in January 2023, under the full influence of Hunga Tonga aerosol, the AOT increased to 0.04–0.05 and the effective radius of the pronounced accumulation mode caused by the volcanic sulfate aerosol was around  
250 250 nm. These Utsteinen AOT observations were found to be in good agreement with our lidar observations at the German Antarctic Neumayer station (about 500 km west of the Utsteinen site) during the first months of 2023. The profile data showed 532 nm AOTs of 0.02–0.025 for the height range from the tropopause up to 20 km. According to the AERONET observations discussed by Boichu et al. (2023), the 500 nm AOT caused by the volcanic aerosol was of the order of 0.3–0.5 and the effective radius of the well-defined accumulation mode was close to 400 nm in January 2022.

### 255 3.3 Downloaded AERONET products and aerosol-type-dependent data filtering

The data downloaded from the AERONET data base for each station in Table 3 are listed in Table 4. The version-3-inversion data files contain AOT values for 440, 675, 870 and 1020 nm, separately for fine-mode and coarse-mode aerosol, and the



260 corresponding particle size distribution for each individual observational data set. Furthermore, the volume and surface-area concentrations, separately for fine-mode and coarse-mode fractions, are available. These products are sufficient to calculate all conversion factors for 532 and 911 nm. From interpolations between neighboring AOT values by using respective Ångström exponents, we obtained the 532 and 911 nm total (fine-mode and coarse-mode), fine-mode, and coarse-mode AOTs. In principle, the version-3-inversion data files with all the AOT information for 440, 675, 870 and 1020 nm can also be used to extrapolate to 355 and 1064 nm in order to create fine-mode, coarse-mode and total AOT data sets for 355 and 1064 nm.

265 However, we chose an alternative pathway and downloaded the directly observed AOTs (Version 3, AOT data in Table 4) in addition. We used the 380 nm and 440 nm AOTs to obtain the 355 nm (total) AOT by extrapolation and the 870 and 1020 nm AOTs to extrapolate to 1064 nm. Then, we computed the coarse-mode AOTs at 355 and 1064 nm via extrapolation by using the coarse-mode AOT information in the version-3-inversion data files (covering the wavelength range from 440 to 1020 nm). Finally, we calculated the difference between the total and the coarse-mode AOTs to obtain the fine mode AOTs at 355 and 1064 nm. Internal checks and comparison between all the total, fine-mode, and coarse-mode AOTs from 355 to 270 1064 nm including the downloaded total, fine-mode, and coarse-mode AOTs (at 440, 675, 870, and 1020 nm) indicated the consistency between all optical data. In these data checks, we took the specific absorption and scattering features of mineral dust and wildfire smoke in the 355–532 nm wavelength range into account. This specific information can not be drawn from the 440–870 nm optical properties (Version 3, inversions, in Table 4) alone and remains thus unconsidered without the additionally downloaded Version-3-AOT data.

275 Afterwards, we selected those 355 and 1064 nm AOT data sets that were closest to the observations for which the microphysical properties were available in the Version-3-inversion files. The residual 355 and 1064 nm AOT data were removed and not considered in the regression analysis.

280 Most conversion factors were computed by using total AOT and respective total (fine + coarse-mode) size distribution data. However, the wildfire smoke and volcanic sulfate conversion factors were determined by using the fine-mode AOTs and the respective microphysical properties computed from the fine-mode part of the size distribution, only. More details to this aspect can be found in Ansmann et al. (2021). The fine-mode data in the AERONET data base cover the full size distributions (well-formed, monomodal accumulation mode) of wildfire smoke and volcanic sulfate particles.

285 It should be emphasized that the fine-mode AOT is almost equal to the total AOT in the case of wildfire and volcanic-sulfate-dominated observations. This means that a potential bias introduced by the derivation of the 355 and 1064 nm coarse-mode AOTs and subsequent subtraction from the total AOTs do not introduce a significant bias in the fine-mode AOT data required to derive the wildfire smoke and volcanic sulfate conversion factors.

290 Note that in the case of all AERONET observations with a strong impact of UTLS aerosols on the measured AOT, only level 1.5 AERONET data are available. These UTLS-aerosol-dominated observations are completely removed and are not part of the level 2.0 data base. Level 1.5 are cloud-screened but not further checked for instrumental biases. Level-2.0 data are available after regular inspection and calibration of the photometers at AERONET topical centers and recalculation of the level 1.5 data by using, e.g., updated filter transmission functions.



**Table 4.** AERONET level 2.0 data downloaded for each selected marine, dust, and continental-haze AERONET station in Table 3. These AERONET products are required to derive the sets of conversion factors for all four lidar/ceilometer wavelengths of 355, 532, 911, and 1064 nm. In the case of stratospheric aerosols (wildfire smoke and volcanic sulfate layers), level 1.5 AOT data and corresponding inversion products are available in the AERONET data base, only.

Downloaded AERONET products	
Version 3, AOT:	observed (total) AOT at 380 nm and 1020 nm
Version 3, inversions:	retrieved total, fine and coarse-mode AOT at 440, 675, 870, and 1020 nm, volume size distribution (22 radius classes), total, fine, and coarse-mode volume concentration

After setting up proper data fields of the total, fine-mode, and coarse-mode AOT and related microphysical inversion products, we can step forward towards the regression analyses. Well defined data sets for pure marine, pure dust, and pure continental haze conditions are needed in the correlation studies to obtain the aerosol-type-dependent conversion factors. We applied the filter options as defined in Table 5 to identify and select all pure marine observations conducted at the 8 marine AERONET stations, the pure dust cases over the 12 desert AERONET stations, and the continental-haze-dominated measurements over the 25 urban and rural continental AERONET sites defined in Table 3. For the sake of completeness, the regression analysis considers dust fine-mode AOTs and the respective dust fine-mode column volume concentrations and, respectively, dust coarse-mode AOTs and dust coarse-mode column volume concentrations to obtain the dust fine-mode and coarse-mode volume conversion factors  $c_{v,df}$  and  $c_{v,dc}$ .

**Table 5.** Data filtering and selection options in the POLIPHON conversion-factor retrievals. In the case of continental, marine and dust aerosol, only AERONET observations that fulfill the listed conditions for the Ångström exponent (AE) and the 532 nm AOT conditions are considered in the statistical analysis. The wildfire-smoke filter options are the same as in Ansmann et al. (2021). Manually selected observations are used in the case of volcanic sulfate layers as described in Sect. 3.2.

Aerosol type	AE (440-870 nm)	AOT (532 nm)
Fresh continental haze	1.6–2.0	0.02–0.5
Aged continental haze	1.1–1.5	0.02–0.5
Marine aerosol	0.2–0.6	0.02–0.06
Mineral dust	–0.5 – 0.3	0.1 – 0.5
Fresh wildfire smoke	see Ansmann et al. (2021)	
Aged wildfire smoke	see Ansmann et al. (2021)	
Fresh volcanic sulfate	Selected observations	
Aged volcanic sulfate	Selected observations	



The Ångström exponent AE for the 440–870 nm wavelength range was used to distinguish the different basic aerosol types. High AE values of 1.6–2.0 indicate urban haze with a large fraction of freshly produced small particles. Lower AE values of 1.1–1.5 indicate aged aerosol ensembles, in most cases a mixture of anthropogenic pollution and soil, road, and industrial dust. Very low and low AE values of  $<0.3$  (mineral dust) and from 0.2–0.6 (marine aerosol) are caused by coarse-mode dominated particle ensembles. Because AE values of 0.2–0.6 can also occur during dust events, we used the 532 nm AOT to distinguish dust from marine observations. Only dust cases with a 532 nm AOT exceeding 0.1 were considered in the statistical regression analyses. Marine AOTs are usually well below 0.07. A clear discrimination option to distinguish dust-dominated and marine-aerosol-dominated observations is important for AERONET stations on the islands of Tenerife (Izaña), Cabo Verde, and Barbados (Ragged Point). The filtering conditions for wildfire smoke were discussed in Ansmann et al. (2021) and in the foregoing section for volcanic sulfate aerosol.

### 3.4 From observations at ambient humidity conditions to dry-aerosol conversion factors

One of the most important aspects to be considered in the regression analyses is the need for dry-aerosol conversion factors in Table 2. However, the AERONET observations are conducted at ambient humidity conditions. As a result of water-uptake, hygroscopic particles in the air are larger at RH of 80% than at RH of 40% when they are dry or almost dry. This increase in particle size must be taken into account in the statistical analyses. The strategy to obtain the dry-aerosol conversion factors from AERONET aerosol data observed at ambient RH conditions is explained in Table 6. In order to be in line with the notation in Table 2 and the general lidar nomenclature (particle extinction coefficient instead of AOT, number, surface, volume, and mass concentration instead of column values of these quantities), we divided all AERONET AOTs and column microphysical products by a typical vertical atmospheric length scale (aerosol layer depth) of 1000 m, and proceed with these data sets within the linear regression studies. This change is considered in Table 6.

The goal is to derive those conversion factors (in column 2 in Table 6) from the regression analysis with  $x_{i,j}(\lambda)$  and  $y_{i,j}$  data sets for swollen aerosol particles (in columns 3 and 4) that can be interpreted as conversion factors for dry particles (in column 1). More details to this topic can be found in Mamouri and Ansmann (2016, 2017).

We may explain our basic data analysis concept by the following examples for continental haze:  $c_{60,c,amb}$  is the obtained conversion factor when applying the linear regression analysis to all data pairs  $\sigma_{c,amb,j}$  and  $n_{60,c,amb,j}$  (with observational running index  $j$  from 1 to  $N_{obs}$ ).  $n_{60,c,amb,j}$  considers all particles with radius  $>60$  nm. We assume a typical RH of 60% during the AERONET observations. The continental pollution particles shrink by about 15–20% when the relative humidity decreases to 40% (dry conditions). This means that  $n_{60,c,amb,j}$  is approximately equal to  $n_{50,c,dry,j}$  and represents the particle number concentrations considering all dry particles with radius  $>50$  nm.

As indicated in Table 6, over polluted continents with a strong fraction of hygroscopic sulfate particles, a small water uptake effects has to be generally considered. Even when the photometer observations over rural and urban AERONET sites are conducted at sunny conditions, an RH of 60% as an RH average value for entire continental planetary boundary layer PBL must be considered. Most of the aerosol (usually more than 80–90% of the tropospheric aerosol content) resides in the boundary



**Table 6.** Data analysis concept to obtain dry-aerosol conversion factors (column 1, dry) from AERONET observations at ambient conditions (index: amb, columns 3 and 4) in the case of marine (m), dust (d), and continental (c) pollution particles. The applied linear regression analysis with the  $x_{i,j}$  and  $y_{i,j}$  data fields (described in Appendix A) then lead to the factors for ambient humidity conditions (column 2, ambient). These derived conversion factors are interpreted as the required dry-aerosol conversion factors assuming a mean RH during the AERONET observations as given in column 5 (RH). Column 6 (Unit) shows the units of the individual conversion factors. All individual regression analysis procedures listed in the table are separately repeated for each individual extinction coefficient data set  $\sigma_{i,amb,j}$  (355 nm),  $\sigma_{i,amb,j}$  (532 nm),  $\sigma_{i,amb,j}$  (911 nm), and  $\sigma_{i,amb,j}$  (1064 nm).

POLIPHON	AERONET	Lin. regression analysis		RH	Unit
dry	ambient	$x_{i,j}(\lambda)$	$y_{i,j}$		
<b>Continental aerosol pollution</b>					
$C_{50,c}$	$C_{60,c,amb}$	$\sigma_{c,amb,j}(\lambda)$	$n_{60,c,amb,j}$	60%	Mm cm <sup>-3</sup>
$C_{250,c}$	$C_{290,c,amb}$	$\sigma_{c,amb,j}(\lambda)$	$n_{290,c,amb,j}$	60%	Mm cm <sup>-3</sup>
$C_{s,c}$	$C_{s,c,amb}/1.33$	$\sigma_{c,amb,j}(\lambda)$	$s_{c,amb,j}/1.33$	60%	Mm μm <sup>2</sup> cm <sup>-3</sup>
$C_{v,c}$	$C_{v,c,amb}/1.5$	$\sigma_{c,amb,j}(\lambda)$	$v_{c,amb,j}/1.5$	60%	Mm μm <sup>3</sup> cm <sup>-3</sup>
<b>Mineral dust</b>					
$C_{60,d}$	$C_{60,d,amb}$	$\sigma_{d,amb,j}(\lambda)$	$n_{60,d,amb,j}$	<50%	Mm cm <sup>-3</sup>
$C_{100,d}$	$C_{100,d,amb}$	$\sigma_{d,amb,j}(\lambda)$	$n_{100,d,amb,j}$	<50%	Mm cm <sup>-3</sup>
$C_{250,d}$	$C_{250,d,amb}$	$\sigma_{d,amb,j}(\lambda)$	$n_{250,d,amb,j}$	<50%	Mm cm <sup>-3</sup>
$C_{s,d}$	$C_{s,d,amb}$	$\sigma_{d,amb,j}(\lambda)$	$s_{d,amb,j}$	<50%	Mm μm <sup>2</sup> cm <sup>-3</sup>
$C_{s,100,d}$	$C_{s,100,d,amb}$	$\sigma_{d,amb,j}(\lambda)$	$s_{100,d,amb,j}$	<50%	Mm μm <sup>2</sup> cm <sup>-3</sup>
$C_{v,d}$	$C_{v,d,amb}$	$\sigma_{d,amb,j}(\lambda)$	$v_{d,amb,j}$	<50%	Mm μm <sup>3</sup> cm <sup>-3</sup>
$C_{v,df}$	$C_{v,df,amb}$	$\sigma_{df,amb,j}(\lambda)$	$v_{df,amb,j}$	<50%	Mm μm <sup>3</sup> cm <sup>-3</sup>
$C_{v,dc}$	$C_{v,dc,amb}$	$\sigma_{dc,amb,j}(\lambda)$	$v_{dc,amb,j}$	<50%	Mm μm <sup>3</sup> cm <sup>-3</sup>
<b>Marine particles</b>					
$C_{50,m}$	$C_{100,m,amb}$	$\sigma_{m,amb,j}(\lambda)$	$n_{100,m,amb,j}$	80%	Mm cm <sup>-3</sup>
$C_{250,m}$	$C_{500,m,amb}$	$\sigma_{m,amb,j}(\lambda)$	$n_{500,m,amb,j}$	80%	Mm cm <sup>-3</sup>
$C_{s,m}$	$C_{s,m,amb}/4$	$\sigma_{m,amb,j}(\lambda)$	$s_{m,amb,j}/4$	80%	Mm μm <sup>2</sup> cm <sup>-3</sup>
$C_{v,m}$	$C_{v,m,amb}/8$	$\sigma_{m,amb,j}(\lambda)$	$v_{m,amb,j}/8$	80%	Mm μm <sup>3</sup> cm <sup>-3</sup>

layer over the polluted continents. As mentioned, at these slightly enhanced humidity conditions the particle radius is about a factor of  $1.15 \pm 0.05$  larger than the dry-particle radius at  $RH < 40\%$  (Skupin et al., 2016).

We assume an even higher marine PBL RH value of 80% over the island stations during the observations of marine aerosols so that we expect a particle radius increase by roughly a factor of 2.0 according to an extinction enhancement factor of 3.7



at 532 nm as observed by Haerig et al. (2017) when RH increased from dry conditions with RH=40% to humid conditions with RH=80%. Such very high enhancement factors close to 4 could be measured in pure marine air over Barbados during the winter season in the absence of any continental influence from Africa, South and Central America.

Water vapor effects are neglected in the case of desert dust observations, RH < 50% is assumed during the sunny AERONET observations at the AERONET stations close to or in deserts. As in the case of desert dust, we also assume dry conditions (RH < 50%) during wildfire smoke and volcanic sulfate observations. Dry conditions generally prevailed in the upper troposphere and lower stratosphere and were probably also given in most cases of AERONET observations of smoke in the lowest 5 km of the troposphere over the AERONET stations in or close to fire regions.

As described in detail in Mamouri and Ansmann (2016, 2017), the respective dry-aerosol surface area concentrations and volume concentrations for continental aerosol pollution (at RH=40%) are a factor of 1.33 and 1.5, respectively, lower than the ambient-condition (RH=60%) surface area and volume concentrations in the case that the particle radius decreases by a factor of 1.15. Similarly, the dry aerosol surface area and volume values are smaller by a factor of 4 and 8 than the observed ones, respectively, when the particle radius shrinks by a factor of 2. These factors are considered in Table 6 (columns 2,3, and 4).

In the case of the conversion factors, used to obtain particle number concentrations, we used a different way to consider the water uptake effect. As shown in Table 6, we simply interpret the computed values of  $n_{60,c,amb,j}$  and  $n_{290,c,amb,j}$  as  $n_{50,c,dry,j}$  and  $n_{250,c,dry,j}$ , respectively, when assuming a particle radius reduction by a factor of 1.15. Similarly for marine aerosol, we assume that the observed values  $n_{100,m,amb,j}$  and  $n_{500,m,amb,j}$  are representative for the respective dry-aerosol values  $n_{50,m,dry,j}$  and  $n_{250,m,dry,j}$ , respectively, when the particle radius is reduced by a factor of 2.

### 3.5 Correction of humidity effects in actual lidar observation

If nearby radiosonde observations are available so that a precise knowledge of the RH profile is given one can, in principle, transfer the continental extinction coefficient measured with lidar at a given RH level to extinction coefficients at 60% in the retrieval of urban and rural continental aerosol microphysical properties, to the extinction coefficient at 80% in the retrieval of the microphysical properties of marine particles, and to extinction values for 40% in the retrieval of dust, smoke and volcanic sulfate microphysical properties before applying the dry-particle conversion factors as given in Table 6. The RH-related transfer of the extinction coefficient can be done following the Hänel parameterization (Hänel, 1976; Skupin et al., 2016; Haerig et al., 2017, 2025b). If radiosonde observations are not available one may use modeled RH profiles. However, these profiles have to be generally handled with caution. Especially during conditions with cloud developments, modeled RH fields may not reflect properly the true RH conditions during the lidar observations. In such complicated cases, we recommend to leave out any humidity correction.

As a further remark, we recommend to avoid the application of the POLIPHON method in cases of lidar observations just below the base of cloud layer, i.e., where RH is of the order >90% so that strong water-uptake by the particles causes large backscatter and extinction coefficients. The use of these large backscatter and extinction coefficients in the POLIPHON computations may lead strong biases (overestimation) in the estimates of the microphysical properties because of the large



**Table 7.** Solutions of the linear regression analysis for intercept  $a_i$  (in  $\text{cm}^{-3}$ ) and slope  $b_i$  (in  $\text{Mm cm}^{-3}$ ), and the ratio  $\overline{y_i}/\overline{x_i}$  (in  $\text{Mm cm}^{-3}$ ) by using  $\sigma_{i,\text{amb},j}$  (532 nm) as  $x_{i,j}$  and  $n_{100,\text{d},\text{amb},j}$  (IZA),  $n_{100,\text{m},\text{amb},j}$  (AMS),  $n_{60,\text{c},\text{amb},j}$  (BEI), and  $n_{60,\text{c},\text{amb},j}$  (PRE) as  $y_{i,j}$ .  $N_{\text{obs}}$  is the number of observed  $x_{i,j}$  and  $y_{i,j}$  data pairs considered in the individual regression analyses.  $R^2$  is the coefficient of determination. The computation of the different quantities, uncertainties  $\delta a$  and  $\delta b$ , and the coefficient of determination  $R^2$  is explained in Appendix A. The correlation studies are performed to obtain the dry-particle POLIPHON conversion factors  $c_{100,\text{d}}$  (IZA),  $c_{50,\text{m}}$  (AMS),  $c_{50,\text{c}}$  (BEI, AE:1.1–1.5) and  $c_{50,\text{c}}$  (PRE, AE:1.6–2.0) as required in Table 2. The  $\overline{y_i}/\overline{x_i}$  values are interpreted as the optimum solution for the sought conversion factors.

Site	$a_i \pm \delta a_i$	$b_i \pm \delta b_i$	$\overline{y_i}/\overline{x_i}$	$N_{\text{obs}}$	$R^2$
Desert dust, $c_{100,\text{d}}$					
IZA	$31.68 \pm 7.336$	$1.250 \pm 0.028$	1.379	447	0.87
Marine aerosol, $c_{50,\text{m}}$					
AMS	$-10.34 \pm 13.51$	$4.065 \pm 0.309$	3.822	91	0.67
Continental pollution, AE: 1.1–1.5, $c_{50,\text{c}}$					
BEI	$-59.15 \pm 34.08$	$16.79 \pm 0.1367$	16.52	1561	0.88
Continental pollution, AE: 1.6–2.0, $c_{50,\text{c}}$					
PRE	$91.03 \pm 37.66$	$16.85 \pm 0.1640$	17.30	1609	0.87

and not well known RH-controlled impact of water uptake effects. We recommend to use only POLIPHON products in aerosol-cloud-interaction studies for heights at least 500 m below the observed cloud base heights (Jimenez et al., 2020).

#### 4 Regression analysis results

The results of the statistical analysis of four contrasting AERONET data sets are discussed in Sect. 4.1 to introduce the basic products of the correlation studies and explain the variability in the results and what statistical quantity best represents the required specific conversion factor. In Sect. 4.2, the conversion factor sets for all individual marine, dust, and continental-pollution AERONET stations are presented and the variability in these conversion factors is discussed. In Sect. 4.3, mean values of all determined conversions factors are presented as a function of aerosol type and wavelength. All in all, 1488 individual regression analyses were performed to obtain 96 different conversion factors (for the 5 aerosol types and 4 wavelengths).

##### 380 4.1 Case studies

Table 7 shows the results of the regression analysis applied to four contrasting AERONET data sets. Desert dust observations (IZA, Izana, Tenerife), a marine case (AMS, Amsterdam Islands) and observations at two urban AERONET stations (BEI, Beijing, China; PRE, Pretoria, South Africa) were used in the correlation studies. As outlined in Appendix A, the applied least-



squares estimation method of fitting the best straight line to data points  $x_{i,j}$  and  $y_{i,j}$  delivers the slope  $b_i$  and the intercept  $a_i$ . In  
 385 our AERONET-based statistical data analysis, slope  $b_i$  is a good proxy for the conversion factor  $c_i$ , describing the relationship  
 between the extinction coefficient ( $x_i$ ) and the microphysical product ( $y_i$ ). Physically, the most reasonable solution for  $b_i$   
 is given when  $a_i \approx 0$ , so that the microphysical values are close to zero when the particle extinction coefficient is close to  
 zero. However, due to the scatter in the  $y_{i,j}$  values, mostly caused by AERONET retrieval uncertainties, the intercept  $a_i$  is  
 larger or lower than 0. Table 7 shows a few examples of solution sets for the intercept  $a_i \pm \delta a_i$  and slope  $b_i \pm \delta b_i$  in the  
 390 case of the linear regression analysis with  $x_{d,j} = \sigma_{d,amb,j}$  at 532 nm and  $y_{d,j} = n_{100,d,amb,j}$  (IZA, dust observations,  $c_{100,d}$   
 retrieval). The Amsterdam Island example uses  $x_{m,j} = \sigma_{m,amb,j}$  at 532 nm and  $y_{m,j} = n_{100,m,amb,j}$  (Amsterdam Island, AMS,  
 marine conditions,  $c_{50,m}$  retrieval). The urban examples are based on the regression analysis with  $x_{c,j} = \sigma_{c,amb,j}$  at 532 nm and  
 $y_{c,j} = n_{60,c,amb,j}$  (BEI, urban haze, AE range: 1.1–1.5, PRE, urban haze, AE range: 1.6–2.0,  $c_{50,c}$  retrieval).

As can be seen, the intercept value  $a_i$  can have a noticeable impact on the solution for  $b_i$ . According to Eq. (A1), the slope  
 395  $b_i$  is equal to  $\bar{y}_i/\bar{x}_i$  when the intercept is  $a_i = 0$ . We see that  $b_i$  is smaller than this ideal  $b_i$  (for  $a_i = 0$ ) when  $a_i$  is positive, and  
 vice versa,  $b_i$  is larger than the ideal  $b_i$  when  $a_i$  is negative. In most cases, it was found that  $a_i$  had only a minor impact on the  
 determination of  $b_i$ , so that  $b_i$  was close to  $\bar{y}_i/\bar{x}_i$  (within about 5% around  $\bar{y}_i/\bar{x}_i$ ) as is the case in Table 7 for the Beijing and  
 Pretoria data.

In Figs. 3 and 4, the results of the Izaña and Beijing data analyses are shown. The different, but similar regression lines  
 400 corroborate that the use of the  $\bar{y}_i/\bar{x}_i$  values as conversion factors is fully justified. Note, that the shown  $c_{50,i}$  and  $c_{100,d}$  retrievals  
 are the most critical ones. The statistical analysis is based on strongly scattered data with a considerable fraction of unwanted  
 outliers. The data are less noisy in the case of the other conversion factors (Mamouri and Ansmann, 2016, 2017; Ansmann  
 et al., 2019b).

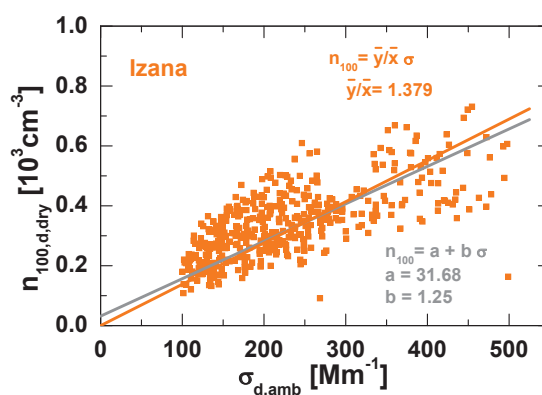


**Figure 3.** Number concentration  $n_{100,d,dry}$  versus dust extinction coefficient  $\sigma_{d,amb}$  (532nm). The regression lines are obtained from the  
 weighed linear regression analysis applied to 447 individual AERONET observations performed at Izaña. Table 7 contains the regression  
 products  $a$ ,  $b$ , and  $\bar{y}/\bar{x}$  which are used to compute the gray and orange regression lines, respectively.

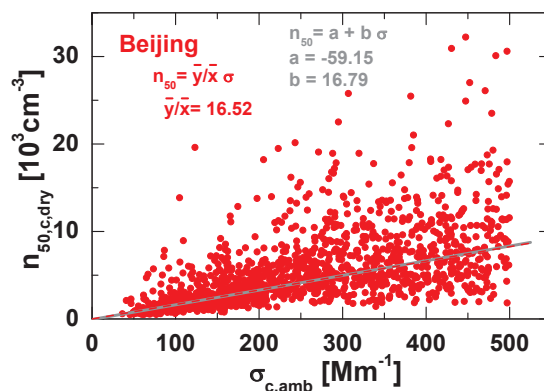


**Figure 4.** Same as Fig. 3, except for continental pollution aerosol observations at Beijing (for the AE range from 1.1–1.5). The statistical analysis is based on 1561 individual observations. The two regression lines (solid gray line, dashed red line) almost coincide and are thus not distinguishable.

In the following tables in Sect. 4.2 and 4.3, we use the values for  $\overline{y_i}/\overline{x_i}$  with the weighted mean values  $\overline{x_i}$  and  $\overline{y_i}$  according to Eqs. (A2) and (A3), respectively, as the conversion factors and interpret them as the dry-aerosol conversion factors that are needed in the main POLIPHON Table 2 to obtain the microphysical properties  $n_{50,i,dry}$ ,  $n_{100,i,dry}$ ,  $n_{250,i,dry}$ ,  $s_{i,dry}$ , and  $v_{i,dry}$ .

## 4.2 Station-by-station analysis

Tables 8–11 show the products of the regression analyses for all AERONET stations. The 532 nm conversion factors are listed. Table 8 contains the dust conversion factors obtained from the analysis of the selected 12 dust AERONET stations. The marine conversion factors in Table 9 are obtained from the regression studies with the observations at the 8 selected marine stations. Tables 10 and 11 show all conversion factors for anthropogenic haze derived from the selected 25 selected continental rural and urban AERONET stations. As already mentioned,  $N_{obs}$  in the four tables is the number of used  $x_{i,j}$  and  $y_{i,j}$  data pairs in the correlation studies and  $R^2$  is the coefficient of determination and indicates the uncertainty in the obtained results. The lowest  $R^2$  values are usually obtained in the  $c_{50,i}$  and  $c_{60,d}$  regression studies. The highest  $R^2$  values are given in the regression analysis to obtain  $c_{s,i}$  and  $c_{v,i}$ .

The station-by-station results in the four tables provide an impression of the variability in the obtained conversion factors for the three main aerosol types. The reasons for the variability are varying ambient humidity conditions during the observations, varying aerosol conditions, especially regarding the size distributions of the observed aerosol mixtures over the polluted continents, and uncertainties in the AERONET inversion products ( $y_{i,j}$  values).

Fairly similar conversion factor sets were obtained for the different stations in the case of pure dust (Table 8) and pure marine observations (Table 9). A less homogeneous picture was obtained from the AERONET observations of anthropogenic pollution (Tables 10 and 11). As a new aspect, we distinguish between continental anthropogenic pollution for the two different AE ranges to better cover conditions with aged and fresh anthropogenic pollution and situations with urban haze and pollution



**Table 8.** 532 nm POLIPHON conversion factors for the dust aerosol type ( $i = d$ ), derived from dust observations at 12 AERONET stations. The full names of the stations are given in Table 3. Units of the conversion factors are given in Table 6.  $N_{\text{obs}}$  is the number of observed  $x_j$  and  $y_j$  data pairs considered in the individual regression analysis.  $R^2$  is the coefficient of determination. Detailed explanations to the conversion factors are provided in Sect. 2.4 and 3.1.

Site	$c_{60,d}$	$c_{100,d}$	$c_{250,d}$	$c_{s,d}$	$c_{s,100,d}$	$c_{v,d}$	$c_{v,dc}$	$c_{v,df}$	$N_{\text{obs}}$	$R^2$
TAM	13.06	2.02	0.181	2.52	1.60	0.650	0.789	0.234	2847	0.79–0.98
SAL	7.33	1.70	0.200	2.06	1.59	0.626	0.766	0.200	2362	0.73–0.97
IZA	10.09	1.38	0.199	2.28	1.51	0.577	0.701	0.206	447	0.83–0.99
RAG	8.21	1.71	0.188	2.08	1.62	0.634	0.762	0.201	488	0.79–0.97
SED	11.81	2.01	0.183	2.43	1.58	0.627	0.778	0.216	1884	0.78–0.98
SOL	14.73	2.92	0.133	2.68	1.70	0.695	0.911	0.216	2237	0.75–0.95
DUS	17.06	2.49	0.117	2.83	1.65	0.802	1.010	0.244	419	0.75–0.96
LZH	13.59	2.08	0.154	2.59	1.63	0.720	0.943	0.194	114	0.56–0.92
WHI	8.29	1.92	0.106	2.20	1.60	1.060	1.110	0.203	52	0.84–0.99
TRE	6.87	1.58	0.148	2.01	1.59	0.875	1.060	0.184	29	0.25–0.96
BIR	11.43	1.49	0.096	2.36	1.59	0.884	1.050	0.226	108	0.82–0.99
GOB	7.18	1.79	0.214	2.03	1.58	0.609	0.808	0.180	158	0.75–0.98

**Table 9.** Same as Table 8, except for the marine aerosol type ( $i = m$ ). The 532 nm POLIPHON conversion factors are derived from observations at 8 marine AERONET sites (island stations, far away from continents, see Fig. 2).

Site	$c_{50,m}$	$c_{250,m}$	$c_{s,m}$	$c_{v,m}$	$N_{\text{obs}}$	$R^2$
RAG	3.23	0.0625	0.552	0.0829	164	0.61–0.86
LAN	3.24	0.0609	0.567	0.0849	327	0.71–0.87
GRA	3.47	0.0653	0.599	0.0868	175	0.72–0.87
NAU	3.36	0.0613	0.560	0.0881	72	0.50–0.78
THA	4.02	0.0618	0.647	0.0850	141	0.62–0.79
MID	3.26	0.0621	0.566	0.0855	120	0.60–0.85
PAG	3.50	0.0592	0.563	0.0866	115	0.49–0.77
AMS	3.82	0.0634	0.585	0.0840	91	0.67–0.89

425 conditions preferably occurring in rural regions. AE of 1.6–2.0 indicates the dominance of freshly produced, relatively small anthropogenic particles whereas AE from 1.1–1.5 suggests a considerable impact of larger particles, i.e., of aged anthropogenic particles including mixtures of fine-mode pollution and coarse-mode particles such as road, soil, and industrial dust. In winter, residential heating including wood burning (Malollari et al., 2025) contributes to the haze over the continents while during other seasons, bioaerosol (pollen, spores) and biological material from agricultural and harvesting activities may dominate the



**Table 10.** Same as Table 8, except for the continental-pollution aerosol type ( $i = c$ ). The 532 nm POLIPHON conversion factors are derived from observations at 25 continental, urban and rural AERONET stations (see Fig. 2). Only 532 nm AOT observations (and corresponding microphysical products) are considered in the statistical analysis showing AE values from 1.1–1.5. These relatively low AE values indicate aged continental pollution particles and the impact of local dust. Further filtering options are given in Table 5.

Site	$c_{50,c}$	$c_{250,c}$	$c_{s,c}$	$c_{v,c}$	$N_{\text{obs}}$	$R^2$
GDL	15.29	0.0925	2.01	0.194	784	0.91–0.95
KUO	12.44	0.0938	1.91	0.164	747	0.92–0.95
WAT	10.48	0.1295	1.83	0.196	243	0.87–0.96
MOS	15.29	0.0790	2.12	0.249	834	0.91–0.96
LEI	11.18	0.1160	1.84	0.200	1325	0.87–0.95
LIL	9.92	0.1301	1.76	0.177	1981	0.88–0.95
DAV	12.69	0.0855	1.85	0.159	191	0.91–0.94
MOD	9.81	0.1213	1.73	0.171	1618	0.87–0.94
VAL	12.82	0.1048	1.92	0.232	3611	0.87–0.94
ATH	13.24	0.0933	1.98	0.232	1611	0.86–0.95
TEL	11.67	0.1075	1.95	0.261	2334	0.95–0.97
CAI	15.19	0.0926	2.20	0.289	2116	0.79–0.90
BEI	16.52	0.0873	2.14	0.262	1561	0.88–0.94
POK	11.25	0.1156	1.80	0.203	3149	0.77–0.88
CHI	18.71	0.1044	2.39	0.220	1863	0.92–0.96
YAK	10.69	0.1020	1.78	0.174	428	0.93–0.97
BAN	14.09	0.1190	2.20	0.222	1036	0.79–0.87
MBI	13.25	0.0873	1.96	0.280	598	0.86–0.93
PRE	17.94	0.0645	2.24	0.294	1802	0.90–0.95
GRE	15.00	0.1040	2.05	0.202	4284	0.91–0.96
SGP	14.76	0.0841	2.05	0.263	2336	0.90–0.96
LOS	13.99	0.1099	1.91	0.242	1924	0.85–0.94
BON	13.99	0.0953	1.92	0.174	300	0.90–0.95
SAO	18.56	0.0960	2.31	0.224	1467	0.87–0.93
CAN	13.82	0.0906	1.99	0.225	2238	0.90–0.96

coarse-mode fraction. In the original study (Mamouri and Ansmann, 2016), we only considered the conversion factors for the  
 430 AE 1.6–2.0 range, but especially at rural sites, the conversion factors for the 1.1–1.5 AE range may be more appropriate to  
 estimate CCN concentrations. The comparison of the conversion factors in Tables 10 and 11 reveals that the conversion factors  
 are typically different by 10–20%. The conversion factors  $c_{50,c}$  and  $c_s$  are lower, and thus  $n_{50,c}$  and  $s_c$  are lower for a given



**Table 11.** Same as Table 10, except for the continental-pollution aerosol type and considering AERONET observations showing AE values from 1.6–2.0. These high AE values indicate fresh pollution, i.e., smaller particles.

Site	$c_{50,c}$	$c_{250,c}$	$c_{s,c}$	$c_{v,c}$	$N_{obs}$	$R^2$
GDL	18.71	0.088	2.65	0.186	876	0.89–0.93
KUO	17.14	0.074	2.50	0.181	822	0.91–0.94
WAT	12.85	0.097	2.11	0.171	31	0.87–0.88
MOS	18.48	0.078	2.57	0.211	1069	0.87–0.93
LEI	13.66	0.086	2.17	0.179	1590	0.87–0.92
LIL	12.40	0.099	2.01	0.178	1362	0.86–0.93
DAV	13.18	0.089	1.86	0.152	267	0.87–0.94
MOD	14.35	0.082	2.18	0.184	2699	0.86–0.93
VAL	14.64	0.086	2.18	0.197	1459	0.85–0.93
ATH	13.60	0.069	2.12	0.196	1975	0.83–0.92
TEL	13.09	0.095	2.20	0.209	189	0.91–0.96
CAI	20.80	0.126	2.95	0.254	31	0.87–0.95
BEI	20.34	0.071	2.53	0.238	94	0.81–0.91
POK	19.54	0.087	2.30	0.193	342	0.85–0.92
CHI	24.11	0.093	2.93	0.202	419	0.87–0.94
YAK	13.56	0.085	2.13	0.135	1352	0.93–0.96
BAN	19.57	0.078	2.70	0.197	772	0.69–0.80
MBI	19.46	0.069	2.53	0.216	53	0.50–0.89
PRE	17.30	0.052	2.36	0.221	1609	0.87–0.92
GRE	14.46	0.085	2.03	0.160	7276	0.90–0.96
SGP	12.88	0.063	2.07	0.199	958	0.93–0.96
LOS	19.48	0.083	2.41	0.246	335	0.93–0.95
BON	15.63	0.085	2.14	0.101	281	0.88–0.96
SAO	21.46	0.067	2.59	0.230	351	0.81–0.91
CAN	15.62	0.065	2.19	0.191	696	0.91–0.95

extinction coefficient, in the case of aerosols mixtures showing AE from 1.1–1.5 compared to the respective values for AE from 1.6–2.0. The opposite is the case for the  $c_{250,c}$  and  $c_{v,c}$  conversion factors.

435 Figures 5 and 6 show the impact of the conversion factor variability on the retrieval of the CCN and dry-aerosol mass concentrations in the case of marine, dusty, and haze conditions. The particle extinction coefficient at 532 nm is set to  $100 \text{ Mm}^{-1}$  and converted into the shown CCN and dry-mass concentration values. As can be seen, a rather low variability in the POLIPHON results and thus in the respective conversion factors is observed in the case of marine particles. Rather homogeneous conditions obviously prevail over the AERONET island stations during pure marine conditions as defined in Table 5. A similar conclusion

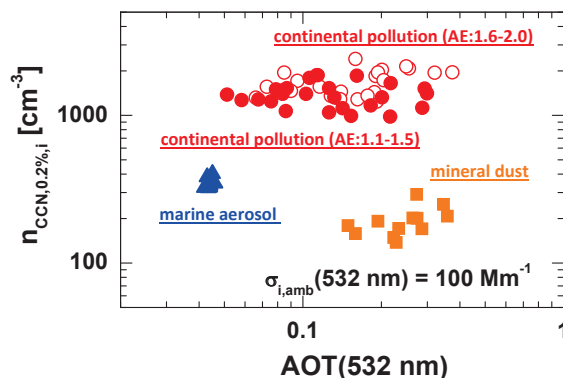


**Figure 5.** Impact of individual, station-by-station conversion factors on the estimated CCN number concentration. A 532 nm particle extinction coefficient  $\sigma_{i,\text{amb}}(532 \text{ nm}) = 100 \text{ Mm}^{-1}$  is converted into  $n_{\text{CCN},0.2\%,i}$  values by using the equations in Table 2. Eight individual marine conversion factors  $c_{50,m}$  are used to compute  $n_{\text{CCN},m}$  (blue triangles), 12 dust conversion factors  $c_{100,d}$  are applied to obtain  $n_{\text{CCN},d}$  (orange squares), and 25 continental-pollution conversion factors  $c_{50,c}$ , derived from AERONET observation with AE from 1.1–1.5 (solid red circles) and from AERONET observations with AE from 1.6–2.0 (open red circles) are used to obtain  $n_{\text{CCN},c}$ . To better visualize the impact of the individual, station-by-station conversion factors, the CCN solutions are shown as a function of the station-mean 532 nm AOT, which is computed from all observations at a given AERONET site that were included in the respective individual conversion-factor determination.

440 can be drawn in the case of desert dust. A stronger variability is observed for anthropogenic haze conditions. One needs to take a 50% uncertainty always into account in CCN estimations.

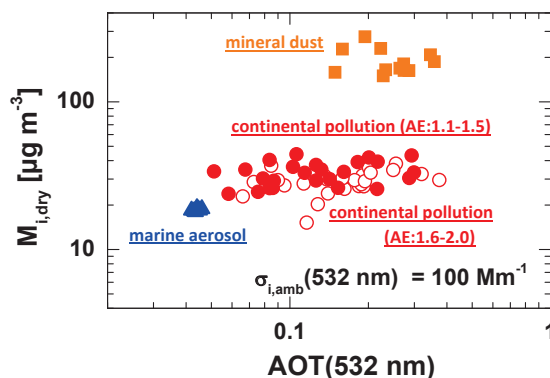


**Figure 6.** Same as Fig. 5, except for the computation of the dry-particle mass concentration from 532 nm particle extinction coefficient  $\sigma_{i,\text{amb}}(532 \text{ nm}) = 100 \text{ Mm}^{-1}$ . The conversion factors  $c_{v,i}$  and particle densities of 2.16 (dry marine), 1.5 (sulfate), and 2.6  $\text{g cm}^{-3}$  (dust) are used.



### 4.3 Analysis summary: Mean conversion factors for 5 aerosol types and 4 wavelengths

Mean values for all conversion factors, for the five aerosol types, and the four wavelengths are presented in Tables 12–14. All station-by-station values, listed in Tables 8–11 were averaged, separately for each conversion factor and aerosol type, to obtain the mean 532 nm conversion factors for the three fundamental aerosol types (marine, dust, continental pollution). In the same way, the data sets of conversion factors for 355, 911, and 1064 nm were processed. The results are shown in Tables 12 and 13. The statistical analyses applied to the wildfire smoke and volcanic sulfate observations lead to the conversion factors given in Table 14.

Table 12 is explicitly presented as support to the dust observations around the globe with CALIOP and ACDL (532 nm laser wavelength) and ALADIN and ATLID (355 nm wavelength). Mean values and standard deviations (SD) are listed. To combine the long-term aerosol observations, performed since 2006, in terms of microphysical properties in a coherent way, an internally consistent conversion factor set as given in Table 12 is required.

**Table 12.** Dust conversion factors (dust cf) for the conversion of  $\sigma_{d,amb}$  (355 nm) and  $\sigma_{d,amb}$  (532 nm) into respective dust particle number, surface area, and volume concentrations. These POLIPHON conversion factors can be used in Table 2. The individual, station-by-station conversion factors of the 12 AERONET dust sites were averaged and the respective mean values are listed.

dust cf	355 nm	532 nm
$c_{60,d}$	$9.04 \pm 2.73$	$10.80 \pm 3.34$
$c_{100,d}$	$1.74 \pm 0.32$	$1.92 \pm 0.43$
$c_{250,d}$	$0.144 \pm 0.04$	$0.160 \pm 0.04$
$c_{s,d}$	$2.11 \pm 0.19$	$2.34 \pm 0.28$
$c_{s,100,d}$	$1.46 \pm 0.03$	$1.61 \pm 0.05$
$c_{v,d}$	$0.653 \pm 0.104$	$0.730 \pm 0.146$
$c_{v,dc}$	$0.962 \pm 0.143$	$0.891 \pm 0.141$
$c_{v,df}$	$0.124 \pm 0.007$	$0.209 \pm 0.019$

Table 13 contains mean values of the four fundamental conversion factors  $c_{50,i}$ ,  $c_{250,i}$ ,  $c_{s,i}$ , and  $c_{v,i}$  for the three basic aerosol types and the four wavelengths. In principle, one can use the individual conversion factor data in Tables 8–11 in cases with lidar and ceilometer observations close to one of the considered stations. However, when comparing ceilometer or lidar network data (on a continental scale), it is recommended to use the mean conversion factors given in Table 13.

The same AERONET data analysis procedure as described above and presented in Tables 8–13 for the marine, dust, and pollution aerosol types, was applied to the wildfire smoke and volcanic sulfate observations. The finally obtained mean values are shown in Table 14. The tropospheric smoke conversion factors were obtained from the analysis of the AERONET observations at Reno, Mongu, Mukdahan, Singapore, and Alta Floresta (listed in Table 3). More details are given in Ansmann et al. (2021). Fresh UTLS wildfire smoke conversion factors were calculated from the stratospheric smoke observations at Yellowknife and Churchill in Canada in August 2017. The measurements of Australian smoke more than 10000 km east of the smoke sources in



**Table 13.** Mean values of POLIPHON conversion factors for the 4 aerosol lidar and ceilometer wavelengths. The conversion factors for the three main aerosol types, derived from observations at 8 marine, 12 dust, and 25 continental-pollution AERONET stations, are averaged. The mean values and corresponding SD values in this table are shown in Fig. 7. The units of the conversion factors are given in Table 6.

Mineral dust (d)				
Wavelength	$c_{100,d}$	$c_{250,d}$	$c_{s,d}$	$c_{v,d}$
355 nm	1.74	0.144	2.11	0.653
532 nm	1.92	0.160	2.34	0.730
911 nm	2.08	0.176	2.60	0.790
1064 nm	2.18	0.182	2.75	0.823
Marine aerosol (m)				
Wavelength	$c_{50,m}$	$c_{250,m}$	$c_{s,m}$	$c_{v,m}$
355 nm	2.74	0.0487	0.468	0.068
532 nm	3.49	0.0621	0.580	0.085
911 nm	4.20	0.0765	0.706	0.105
1064 nm	4.49	0.0797	0.750	0.110
Continental haze (c), AE: 1.1–1.5				
Wavelength	$c_{50,c}$	$c_{250,c}$	$c_{s,c}$	$c_{v,c}$
355 nm	7.56	0.0556	1.16	0.130
532 nm	13.70	0.100	1.99	0.220
911 nm	25.72	0.191	3.99	0.448
1064 nm	30.52	0.224	4.79	0.538
Continental haze (c), AE: 1.6–2.0				
Wavelength	$c_{50,c}$	$c_{250,c}$	$c_{s,c}$	$c_{v,c}$
355 nm	8.15	0.0419	1.22	0.104
532 nm	16.65	0.0821	2.34	0.193
911 nm	36.92	0.198	5.60	0.486
1064 nm	47.22	0.253	7.31	0.620

Australia, originating from strong bush fires in December 2019 and January 2020, at the AERONET stations in South America (Punta Arenas, CEILAP RG) and Antarctica (Marambio) were used to determine the conversion factors for aged UTLS wildfire smoke (Ansmann et al., 2021). 465

The observations at the 6 AERONET stations Windpoort, Gobabeb, Metsi, Maido, SP-Each, and PSDA, listed in Table 3 and suggested by Boichu et al. (2023), were used to determine conversion factors for fresh volcanic sulfate layers. These layers



**Table 14.** Same as Table 13, except for wildfire smoke (BB smoke) and volcanic sulfate aerosol. The mean values and corresponding SD values are shown in Fig. 8.

BB smoke, lower troposph. (bb, trop)				
Wavelength	$c_{50,bb}$	$c_{250,bb}$	$c_{s,bb}$	$c_{v,bb}$
355 nm	8.50	0.0973	1.69	0.091
532 nm	15.35	0.326	3.00	0.161
911 nm	44.70	0.498	8.77	0.466
1064 nm	65.22	0.718	12.81	0.674
BB smoke, UTLS, fresh (bb, strat, fresh)				
Wavelength	$c_{50,bb}$	$c_{250,bb}$	$c_{s,bb}$	$c_{v,bb}$
355 nm	6.37	0.120	1.45	0.087
532 nm	10.87	0.187	2.36	0.133
911 nm	27.63	0.498	6.07	0.382
1064 nm	36.58	0.726	7.20	0.519
BB smoke, UTLS, aged (bb, strat, aged)				
Wavelength	$c_{50,bb}$	$c_{250,bb}$	$c_{s,bb}$	$c_{v,bb}$
355 nm	6.37	0.306	1.45	0.098
532 nm	7.33	0.390	1.98	0.126
911 nm	12.93	0.673	3.85	0.276
1064 nm	18.53	0.912	5.14	0.361
Volcanic sulfate, stratosph., fresh (vs, strat, fresh)				
Wavelength	$c_{50,vs}$	$c_{250,vs}$	$c_{s,vs}$	$c_{v,vs}$
355 nm	4.30	0.411	1.34	0.130
532 nm	4.74	0.504	1.55	0.158
911 nm	8.80	0.835	2.24	0.255
1064 nm	10.79	1.055	2.52	0.318
Volcanic sulfate, stratosph., aged (vs, strat, aged)				
Wavelength	$c_{50,vs}$	$c_{250,vs}$	$c_{s,vs}$	$c_{v,vs}$
355 nm	-	-	-	-
532 nm	5.38	0.485	1.70	0.147
911 nm	10.39	0.987	3.33	0.288
1064 nm	13.88	1.322	4.41	0.380

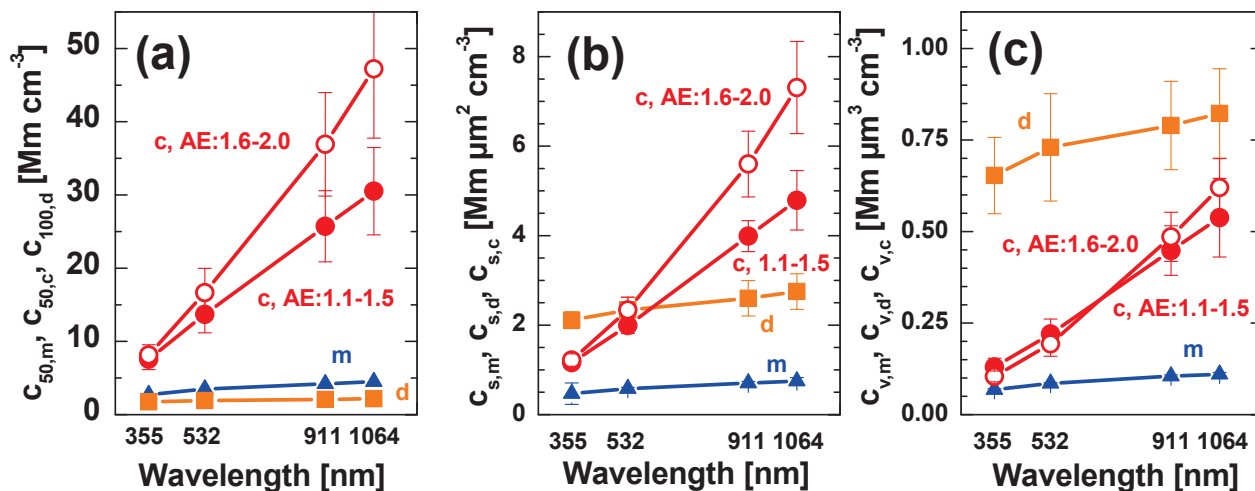


**Figure 7.** POLIPHON conversion factors (mean and SD) as a function of wavelength. (a)  $c_{50,m}$  (blue),  $c_{50,c}$  (solid red circles for AE from 1.1–1.5), open red circles for AE from 1.6–2.0), and  $c_{100,d}$  (orange), (b) same as (a) except for  $c_{s,i}$  with  $i=m, c,$  and  $d$ , and (c) same as (b) except for  $c_{v,i}$ . The values in Table 13 are shown together with SD (error bars).

were observed during the first two weeks after the eruption of the Hunga Tonga volcano. Large AOTs of 0.3–0.5 and large sulfate particles with a particle effective radius of around 400 nm prevailed to that time.

470 The Antarctic observations at the AERONET station of Utsteinen in January 2023 (one year after the eruption) were used to determine the conversion factors for aged volcanic sulfate size distributions, affected by sedimentation and tropopause-fold-related removal processes (Ansmann et al., 1997). The effective radius of the remaining volcanic sulfate particles was reduced to values around 250 nm after one year of long-range transport and the stratospheric contribution to the overall 532 nm AOT was about 0.02, in good agreement with our Antarctic lidar observations in the first half of 2023 (Radenz et al., 2024). For  
 475 355 nm, no useful results could be obtained. The main reason is that the determination of the stratospheric 355 nm AOT via extrapolation by using the observed 380 and 440 nm AOTs was not reliable.

Figures 7 and 8 provide an overview of the wavelength dependence of the mean conversion factors  $c_{50,i}$ ,  $c_{s,i}$ , and  $c_{v,i}$ . The mean values in the Tables 12–14 are shown together with the respective SD (one standard deviation). The vertical SD bars thus indicate the variability in the station-by-station conversion factors. In the case of the Utsteinen conversion factors, we use the  
 480 uncertainty  $\delta b_{vs}$  in the slope  $b_{vs}$  obtained from the regression analysis to indicate the potential uncertainty in the conversion factors.

The wavelength dependence of the conversion factors is directly related to the wavelength dependence of the particle extinction coefficient (or AERONET AOT) of the different aerosol types. The wavelength dependence is low for coarse-mode-dominated dust and marine aerosols and high for fine-mode-dominated aerosol ensembles (haze, smoke, and volcanic sulfate  
 485 aerosols).

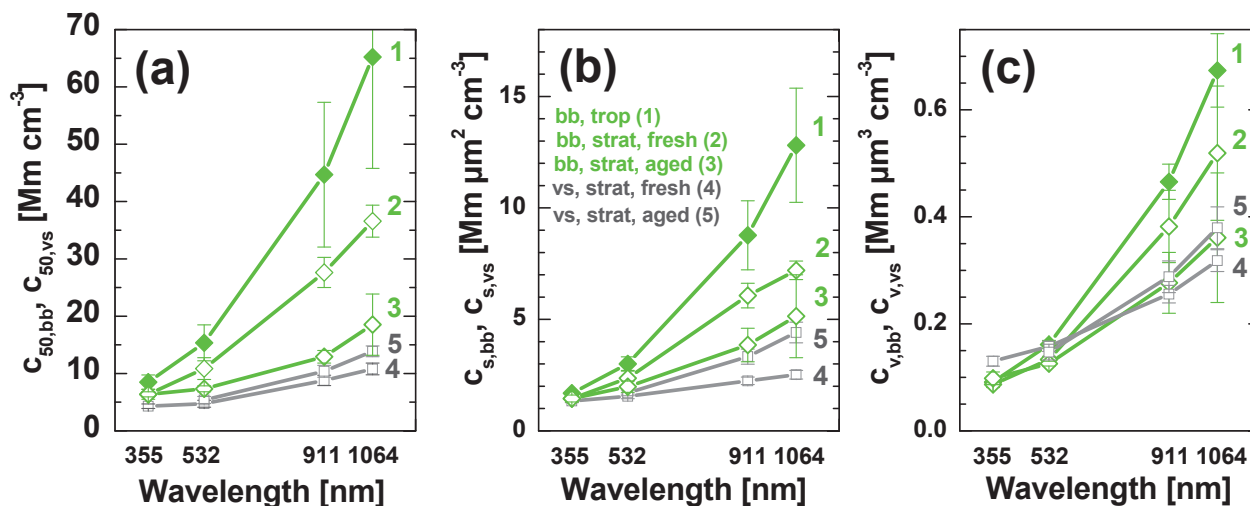


**Figure 8.** Same as Fig. 7, except for wildfire smoke (bb) and volcanic sulfate layers (vs). The values in Table 14 are shown together with SD (error bars).

#### 4.4 Discussion: Comparison of updated (2026) with previous (2016, 2019) conversion factors and conversion factors from alternative retrievals

The most critical conversion, associated with potentially large uncertainties, is the conversion of extinction coefficients into CCN concentrations. However, this approach is an important analysis tool in field studies of aerosol-cloud interaction. In this  
 490 final subsection, we provide comparisons of the updated extinction-to-CCN conversion method with our previous conversion approach (Mamouri and Ansmann, 2016; Ansmann et al., 2019b) and with a few similar alternative conversion efforts (Choudhury et al., 2022; Lenhardt et al., 2023).

In Figs. 9 and 10, we show the relationship between the estimated dry-state particle number concentration  $n_{50,m,dry}$ ,  $n_{50,c,dry}$ , and  $n_{100,d,dry}$  (used as proxy for  $n_{CCN}$ ) and the respective 532 nm particle extinction coefficient  $\sigma_{m,amb}$ ,  $\sigma_{c,amb}$ , and  
 495  $\sigma_{d,amb}$ , measured at ambient humidity conditions with RH of typically 60% (continental aerosol), 80% (marine environment) and <50% (dry desert conditions). The number-vs-extinction relationships are defined by the linear equation  $n_{dry} = c \times \sigma_{amb}$  with conversion factor  $c$  in Figs. 9 and 10 in the case of the A26 curves (this study) and the C22 curves in Fig. 10 (Choudhury et al., 2022). In the case of our previous studies (Mamouri and Ansmann, 2016; Ansmann et al., 2019b) as well as in the study of H25 (He et al., 2025a), the estimation is based on the relationship  $n_{dry} = c \times \sigma_{amb}^{x_p}$  with the additional extinction exponent  
 500  $x_p$  as input.  $x_p$  results from the linear regression with data in the log scale and is typically between 0.75 and 1.

The comparison of the different curves in Figs. 9 and 10 allows us to discuss the differences between the different conversion factors  $c_{50,m}$ ,  $c_{50,c}$ , and  $c_{100,d}$  or, more general, the different conversion approaches when keeping the impact of the varying particle extinction exponent  $x_p$  into account.

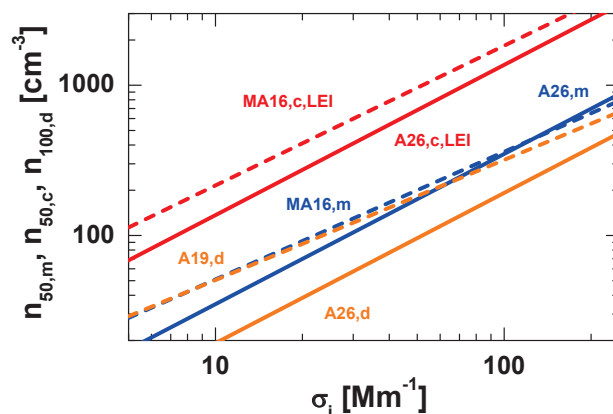


**Figure 9.** Particle number concentration (CCN proxy, dry particles) estimated from the 532 nm particle extinction coefficient by using the 2016 conversion method (MA16,m, marine, blue dashed; MA16,c,LEI, Leipzig urban haze, red dashed; A19,d, dust, orange dashed) (Mamouri and Ansmann, 2016; Ansmann et al., 2019b) and the new linear extinction-vs-number relationship (A26,m; A26,c,LEI; A26,d, solid lines), presented in this study (with the marine and dust conversion factors given in Table 13, and the Leipzig conversion factors in Table 11).

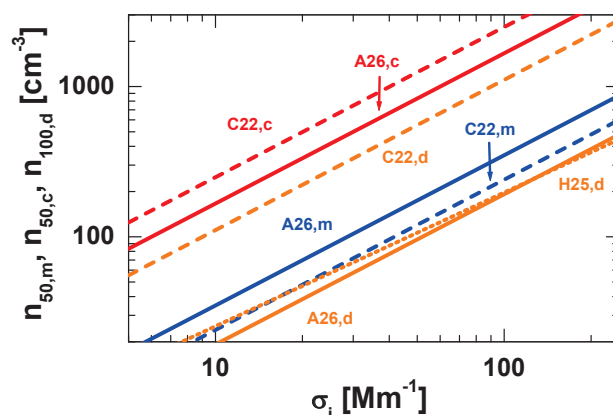


**Figure 10.** Comparison of the linear CCN-vs-extinction relationships applied by C22 (Choudhury et al., 2022) to estimate CCN concentrations from 532 nm extinction coefficients in the case of marine (C22,m, blue dashed), continental pollution (C22,c, red dashed), and dust particles (C22,d, orange dashed) and the respective relationships presented in this study (A26,m; A26,c; A26,d, solid lines, with the 532 nm conversion factors in Table 13). The dotted orange line shows the dust parameterization of He et al. (2025a), indicated by H25,d, derived from observations at a Saudi Arabian AERONET station.

The differences between the curves in Fig. 9 for a given aerosol type are to a large extent related to the changed statistical analysis applied to the AERONET observations. In our original approach (Mamouri and Ansmann, 2016; Ansmann et al., 2019b), we followed the recommendation of Shinozuka et al. (2015) and derived the respective extinction-to-CCN conversion



factors from a linear correlation between, e.g.,  $\log(\sigma_{c,amb,j})$  and  $\log(n_{60,c,amb,j})$  (see Table 6). Now, a weighted linear regression analysis is applied to the data fields of  $\sigma_{i,amb,j}$  and  $n_{60,c,amb,j}$ ,  $n_{100,m,amb,j}$ ,  $n_{60,d,amb,j}$ , or  $n_{100,d,amb,j}$ . This approach is much more simple and efficiently removes outliers. This change in the AERONET data analysis reduces the conversion factors by a factor of 1.4 to 1.8 (for extinction coefficients of 20–50  $\text{Mm}^{-1}$ ) in the case of continental pollution with Leipzig conversion factors (AE range from 1.6–2.0). The new approach significantly improved the POLIPHON conversion factors, which are now better in line with alternative conversion factors discussed by Kulkarni et al. (2025). In the case of mineral dust (A19,d vs A26,d), the conversion factors decreased by roughly a factor of 2 for dust extinction coefficients from 20–50  $\text{Mm}^{-1}$ . Here, the problems with AERONET observations at high dust AOTs  $>0.5$ , as discussed in Ansmann et al. (2019b), may have contributed to the strong deviation between the A19,d and A26,d curves. The MA16,m and A26,m curves for marine conditions are likewise close together. The remaining difference may indicate the impact of the different statistical analysis concepts, following Shinozuka et al. (2015) in the case of MA16,m and by applying the new linear regression approach in the case of A26,m.

In Fig. 10, we compare the updated POLIPHON approach to estimate CCN concentrations from lidar observations (A26,m; A26,c; A26,d) with an alternative approach (C22,m; C22,c; C22,d) introduced by Choudhury and Tesche (2022) and further discussed in Choudhury et al. (2022). In addition, we compare our updated CCN estimations (A26,i) with a parameterization for dust CCN ( $n_{100,d}$ ) suggested by He et al. (2025a), indicated by He25,d and derived from AERONET observations in Saudi Arabia.

The C22 curves are based on conversion factors which are computed by using a specific particle size distribution for each aerosol type (dust, marine aerosol, polluted continental conditions). The microphysical properties for six different aerosol types of the CALIPSO aerosol model (CAMel) are used (Omar et al., 2005, 2009). CALIPSO stands Cloud-Aerosol Lidar and Infrared Pathfinder Satellite Observation (Winker et al., 2009, 2010). The differences between the curves for a given aerosol type  $i$  in Fig. 10 are mainly caused by the differences between the modeled CALIPSO size distribution and the climatological, real-world-reflecting size distributions for marine, dust, and continental haze aerosol derived from the AERONET long-term observations as used in our POLIPHON studies. The strong discrepancy between the dust conversion factors introduced by the underlying mineral dust size distribution characteristics was already discussed by He et al. (2025a). Obviously, the dust fine-mode fraction (particles with radius  $<500$  nm) of the CALIPSO aerosol model contains too many particles. The derived number concentration  $n_{100,d,dry}$  is a factor of 6–7 larger than the respective A26,d values for extinction coefficients of 20–50  $\text{Mm}^{-1}$ . Note, that our previous CCN estimation approach (Mamouri and Ansmann, 2016) already reproduced well airborne in-situ measured CCN concentrations as was shown in Choudhury et al. (2022).

A dust curve provided by He et al. (2025a), derived from AERONET observations in Saudi Arabia, is shown in Fig. 10 in addition. These authors used a different approach to filter out pure or almost pure dust observation. They used the depolarization information in the AERONET data base to filter out the observations dominated by dust. As can be seen, a very good agreement is found although the Shinozuka et al. (2015) approach is used, i.e., the retrieval of the extinction-to- $n_{100}$  conversion factor is based on the correlation between  $\log(\sigma_{d,j})$  and  $\log(n_{100,d,j})$ . This approach provides higher CCN concentrations at lower extinction at lower extinction coefficients.



Lenhardt et al. (2023) studied the relationship between in-situ-measured CCN concentrations in biomass burning smoke layers over the southeastern Atlantic west of southern Africa and 532 nm particle extinction coefficients measured simultaneously with lidar and found conversion factors  $c_{50,bb}$  close to  $10 \text{ Mm cm}^{-3}$ . This is in reasonable agreement with our updated wildfire smoke conversion factors of  $15.4 \text{ Mm cm}^{-3}$  (for the mixture of fresh and aged tropospheric smoke),  $10.9 \text{ Mm cm}^{-3}$  (for fresh smoke in the UTLS) and  $7.3 \text{ Mm cm}^{-3}$  (aged smoke in the UTLS). The biomass burning smoke layers, observed west of Africa, may have even contained some dust particles contributing with rather low conversion factors of around  $2 \text{ Mm cm}^{-3}$  (Table 13) to the overall conversion factor.

Veselovskii et al. (2025) provided an independent multiwavelength-lidar-based approach to derive extinction-to-surface-area and extinction-to-volume conversion factors for aged wildfire smoke at 355 and 532 nm. These authors found  $c_{s,bb}$  of  $1.3 \text{ Mm } \mu\text{m}^2 \text{ cm}^{-3}$  and  $c_{v,bb}$  of  $0.085 \text{ Mm } \mu\text{m}^3 \text{ cm}^{-3}$  for 355 nm and  $1.75 \text{ Mm } \mu\text{m}^2 \text{ cm}^{-3}$  and  $0.13 \text{ Mm } \mu\text{m}^3 \text{ cm}^{-3}$  for 532 nm. Our updated 532 nm conversion factors are  $1.98 \text{ Mm } \mu\text{m}^2 \text{ cm}^{-3}$  and  $0.13 \text{ Mm } \mu\text{m}^3 \text{ cm}^{-3}$ , respectively.

Jäger and Deshler (2002, 2003) published conversion factors for the estimation of surface area concentrations in stratospheric sulfate layers after the strong volcanic eruption of the Pinatubo volcano in 1991. By combining balloon-borne observations of the stratospheric particle size distribution at Laramie, Wyoming, and lidar observations at Garmisch-Partenkirchen, Germany, a few months after the eruption Jäger and Deshler (2003) obtained for  $c_{s,vs}$  at 532 nm values of  $2.5\text{--}3 \text{ Mm } \mu\text{m}^2 \text{ cm}^{-3}$ . We obtained values of  $1.55 \text{ Mm } \mu\text{m}^2 \text{ cm}^{-3}$  very shortly after the eruption of the Hunga Tonga volcano for very fresh sulfate layers, when the impact of sedimentation of sulfate particles only played a minor role. One year later, we derived a value of  $c_{s,vs}=1.7 \text{ Mm } \mu\text{m}^2 \text{ cm}^{-3}$ , when sedimentation and tropopause-fold events already removed the largest sulfate particles. For background conditions, the stratospheric sulfate conversion factors take values of  $4\text{--}6 \text{ Mm } \mu\text{m}^2 \text{ cm}^{-3}$  (Jäger and Deshler, 2003).

## 5 Summary and concluding remarks

An updated set of POLIPHON conversion factors, applicable to lidar and ceilometer observations at the laser wavelengths of 355, 532, 911, and 1064 nm, has been presented. These conversion factors cover five aerosol types. In the case of volcanic ash (type number 6), the dust conversion factors can be used in conversion computations. A broad spectrum of robust, spectrally resolved, real-world-reflecting conversion factors is available for the use in the analysis of ceilometer and lidar network observations and spaceborne lidar data collected in the framework of several space lidar missions since 2006. To obtain the presented set of aerosol-type-dependent conversion factors measurements taken at 60 carefully selected AERONET stations, located in rather different environments around the globe, with data records typically covering 10–20 years, were statistically analyzed.

The main motivation for the update was given by the demands of the ceilometer and space lidar communities. By using the POLIPHON data analysis scheme, the ceilometer product spectrum can be significantly broadened towards CCN, INP, and mass concentration information. This potential may be used to support aerosol emission and transport modeling and weather predictions performed by environmental and meteorological services. Seifert et al. (2023) pointed out that actual



aerosol conditions are not considered at all in numerical weather prediction models so that, e.g., strong Saharan dust outbreaks  
575 towards Europe, North America or Central and East Asia, which may have a strong impact on ice formation in the atmosphere,  
are completely ignored in weather forecasts. Meanwhile, powerful ceilometers are able to monitor desert dust outbreaks in  
large detail and, by using the POLIPHON method, even in terms of CCN and INP concentration estimates.

With respect to atmospheric research with focus on field studies of aerosol-cloud interaction, the updated POLIPHON  
conversion factors may contribute to a more robust and accurate characterization of the aerosol in terms of CCN and INP  
580 concentrations in the framework of closure studies, in which CCN and INP concentrations are compared with cloud droplet  
and ice crystals number concentrations obtainable from combinations of lidar and radar observations of cloud systems. Closure  
studies are of fundamental importance to better understand the impact of different aerosol and meteorological conditions on  
cloud and precipitation formation processes. Such closure studies are also possible from space, e.g., in the framework of the  
EarthCARE mission, so that a global view on aerosol-cloud interaction can in principle be reached with strong support by the  
585 POLIPHON methodology.

#### Appendix A: Conversion factors from LSE studies

The least-squares estimation (LSE) method (York et al., 2004) is applied to determine all conversion factors mentioned in  
Table 6. The respective input data sets  $x_{i,j}$  (particle extinction coefficient for aerosol type  $i$  and observations  $j$  from  $j = 1$  to  
 $j = N_{\text{obs}}$ ) and  $y_{i,j}$  (one of the retrieved microphysical aerosol products for aerosol type  $i$ ) are given in Table 6 ( $x_{i,j}$  and  $y_{i,j}$   
590 columns).

For simplicity, we continue with  $x_j$  and  $x_j$  in this appendix, and leave out aerosol-type index  $i$ . The classical regression  
scenario is assumed (see Appendix D in York et al., 2004), i.e., we assume that the scatter of data points in the regression plots  
and in the obtained regression results are mainly caused by the uncertainty in the  $y_j$  data and not by the uncertainty in the  
observations  $x_j$ . We assume small uncertainties in  $x_j$  of 10% or less. Such small uncertainties are confirmed by our numerous  
595 lidar-sunphotometer intercomparisons we performed since more than 20 years. In contrast, large uncertainties of 20% to 75%  
are given for the AERONET products (Gerasopoulos et al., 2007; Dubovik and King, 2000; Dubovik et al., 2000, 2002, 2006).

The following set of equations are used to determine the conversion factors (York et al., 2004):

$$\bar{y} = a + b\bar{x}, \tag{A1}$$

$$\bar{x} = \frac{\sum_{j=1}^N w_j x_j}{\sum_{j=1}^N w_j}, \tag{A2}$$

$$\bar{y} = \frac{\sum_{j=1}^N w_j y_j}{\sum_{j=1}^N w_j}, \tag{A3}$$



$$b = \frac{\sum_{j=1}^N w_j \Delta x_j \Delta y_j}{\sum_{j=1}^N w_j \Delta x_j^2}, \quad (\text{A4})$$

605

$$a = \bar{y} - b\bar{x} \quad (\text{A5})$$

with the intercept  $a$ , the regression coefficient  $b$ , the mean value  $\bar{x}$  of the independent variable, the mean value  $\bar{y}$  of the dependent variable, and  $\Delta x_j = x_j - \bar{x}$  and  $\Delta y_j = y_j - \bar{y}$ . The determination of the weights  $w_j$  is explained below. The weights are used to widely suppress the impact of outliers in the  $y_j$  data set on the regression results, especially on the determination  
 610 of the regression coefficient  $b$ .

The conversion factors are approximately given by the regression coefficient  $b$ , provided that the intercept  $a$  is close to zero. For  $a = 0$ ,  $b = \bar{y}/\bar{x}$  according to Eq. A1. The scatter in the  $y_j$  data causes  $a \neq 0$ .

The uncertainties of  $a$  and  $b$  are given by (York et al., 2004)

$$\delta a = \sqrt{\sum_{j=1}^N 1/(w_j) + \bar{x}^2 \delta b^2} \quad (\text{A6})$$

615 and

$$\delta b = \sqrt{1/\sum_{j=1}^N (w_j \Delta x_j^2)} \quad (\text{A7})$$

The coefficient of determination  $R^2$  of the linear regression analysis is given by

$$R^2 = 1 - \frac{\sum_{j=1}^N w_j (y_j - \beta x_j)^2}{\sum_{j=1}^N w_j \Delta y_j^2} \quad (\text{A8})$$

with

$$\beta = \frac{\sum_{j=1}^N w_j x_j y_j}{\sum_{j=1}^N w_j x_j^2}. \quad (\text{A9})$$

The coefficient of determination  $R^2$  expresses how well the dependent variable can be predicted by the observed, independent variable.

The required weights  $w_j$  in Eqs. (A2)–(A4) are obtained in the following way. We transferred all individual ratios  $r_j = y_j/x_j$  to  $r_j = y_{j,\text{ref}}/x_{\text{ref}}$ , i.e., we relate all individual  $y_j$  values to the mean value  $x_{\text{ref}} = \frac{1}{N} \sum_{j=1}^N x_j$ .  $N$  is the number of available  
 625 observations. The transferred values  $y_{j,\text{ref}}$  are given by

$$y_{j,\text{ref}} = \frac{y_j}{x_j} \times x_{\text{ref}}. \quad (\text{A10})$$



Next, we defined the deviation

$$\Delta y_{j,\text{ref}} = y_{j,\text{ref}} - \overline{y_{\text{ref}}} \quad (\text{A11})$$

with the mean value  $\overline{y_{\text{ref}}} = \frac{1}{N} \sum_{j=1}^N y_{j,\text{ref}}$ . The weight is then given by (York et al., 2004)

$$630 \quad w_j = \frac{1}{(\Delta y_{j,\text{ref}})^2}. \quad (\text{A12})$$

To avoid a too large impact of the data points  $y_{j,\text{ref}}$  close to the mean value  $\overline{y_{\text{ref}}}$  on the regression results because of the increasing weight with decreasing distance to  $\overline{y_{\text{ref}}}$ , we set the weight to

$$w_j = \frac{1}{(y_{j,\text{ref}} * 0.1)^2} \quad (\text{A13})$$

if the relative deviation  $\Delta y_{j,\text{ref}}/y_{j,\text{ref}}$  is between 0 and  $\pm 0.1$ . Now, we can compute an improved mean value,

$$635 \quad \overline{y_{\text{ref}}} = \frac{\sum_{j=1}^N w_j y_{j,\text{ref}}}{\sum_{j=1}^N w_j}. \quad (\text{A14})$$

In the following, we may apply Eqs. (A11)–(A14) many times before we proceeded with the regression analysis by using Eqs. (A1)–(A5).

### Data availability

The basic AERONET products are downloaded from <http://aeronet.gsfc.nasa.gov/> (AERONET, 2026).

640 All the analysis products are available at TROPOS upon request (hofer@tropos.de). They are also publicly available in Zenodo at <https://doi.org/10.5281/zenodo.>—— (in progress) (Hofer et al., 2026).

### Author contributions

The paper was written and designed by AA with support by JH, REM, MH, and HB. The computation of the conversion factors was conducted by AA. All coauthors were actively involved in the extended discussions and the elaboration of the final design  
645 of the manuscript.

### Competing interests

Ulla Wandinger is a member of the editorial board of Atmospheric Measurement Techniques

### Financial support

We gratefully acknowledge the European Space Agency (ESA) for the AIRSENSE (Aerosol and aerosol-cloud Interaction from  
650 Remote SENSing Enhancement) project through the contract 4000142902/23/I-NS in the framework of the ESA Atmosphere Science Cluster – Research Opportunities 5 – European Coordinated Study on Aerosols and Aerosol/Cloud Interactions.



We acknowledge the ESA funding through the contract 4000144997/24/I-NS in the framework of the EarthCARE Data, Innovation and Science Cluster (DISC).

This research has been supported by the German Federal Ministry for Economic Affairs and Energy (BMWi) (grant no. 50EE2403A) in the framework of the German Initiative for the Validation of EarthCARE (GIVE).

The authors acknowledge the 'EXCELSIOR': ERATOSTHENES: EXcellence research Centre for Earth Surveillance and Space-Based Monitoring of the Environment H2020 Widespread Teaming project ([www.excelsior2020.eu](http://www.excelsior2020.eu)). The 'EXCELSIOR' project has received funding from the European Union's Horizon 2020 research and innovation programme under Grant Agreement No 857510, from the Government of the Republic of Cyprus through the Directorate General for the European Programmes, Coordination and Development and the Cyprus University of Technology.

This activity has received funding from the European Union's Horizon 2020 research and innovation programme through the ATMO-ACCESS Integrating Activity under grant agreement no. 101008004.

This research has been supported by the German Federal Ministry of Research, Technology and Space (BMFTR) formerly known as German Federal Ministry of Education and Research (BMBF) under the FONA Strategy "Research for Sustainability" (grant no. 01LK2001A).

This project has received funding from the European Union's Horizon 2020 research and innovation program ACTRIS-2 Integrating Activities (H2020-INFRAIA-2014 - 2015, grant agreement no. 654109).

*Acknowledgements.* We gratefully thank the AERONET team, especially the PIs and Co-Is and their staff of the 60 selected stations, for establishing, organizing, and maintaining the sites and providing the high quality data used in this study. We appreciate the well designed and carefully maintained AERONET webpage.

We thank Marie Boichu, LOA, University of Lille, France, for personal communication regarding the specific AERONET observations after the Hunga Tonga–Hunga Ha'apai volcanic eruption.



## References

- AERONET(2026): Aerosol Robotic Network aerosol data base, available at: <http://aeronet.gsfc.nasa.gov/>, last access: 10 January, 2026.
- 675 Alpert, P. A. and Knopf, D. A.: Analysis of isothermal and cooling-rate-dependent immersion freezing by a unifying stochastic ice nucleation model, *Atmospheric Chemistry and Physics*, 16, 2083–2107, <https://doi.org/10.5194/acp-16-2083-2016>, 2016.
- Amarillo, A. C., Curci, G., De Santis, D., Bassani, C., Barnaba, F., Rémy, S., Di Liberto, L., Oxford, C. R., Windwer, E., and Del Frate, F.: Validation of aerosol chemical composition and optical properties provided by Copernicus Atmosphere Monitoring Service (CAMS) using ground-based global data, *Atmospheric Environment*, 334, 120 683, <https://doi.org/10.1016/j.atmosenv.2024.120683>, 2024.
- 680 Ansmann, A., Mattis, I., Wandinger, U., Wagner, F., Reichardt, J., and Deshler, T.: Evolution of the Pinatubo aerosol: Raman lidar observations of particle optical depth, effective radius, mass, and surface area over Central Europe at 53.4°N, *Journal of the Atmospheric Sciences*, 54, 2630–2641, [https://doi.org/10.1175/1520-0469\(1997\)054<2630:EOTPAR>2.0.CO;2](https://doi.org/10.1175/1520-0469(1997)054<2630:EOTPAR>2.0.CO;2), 1997.
- Ansmann, A., Tesche, M., Groß, S., Freudenthaler, V., Seifert, P., Hiebsch, A., Schmidt, J., Wandinger, U., Mattis, I., Müller, D., and Wiegner, M.: The 16 April 2010 major volcanic ash plume over central Europe: EARLINET lidar and AERONET photometer observations at  
685 Leipzig and Munich, Germany, *Geophysical Research Letters*, 37, L13 810, <https://doi.org/10.1029/2010GL043809>, 2010.
- Ansmann, A., Tesche, M., Seifert, P., Groß, S., Freudenthaler, V., Apituley, A., Wilson, K. M., Serikov, I., Linné, H., Heinold, B., Hiebsch, A., Schnell, F., Schmidt, J., Mattis, I., Wandinger, U., and Wiegner, M.: Ash and fine-mode particle mass profiles from EARLINET-AERONET observations over central Europe after the eruptions of the Eyjafjallajökull volcano in 2010, *Journal of Geophysical Research: Atmospheres*, 116, D00U02, <https://doi.org/10.1029/2010JD015567>, 2011.
- 690 Ansmann, A., Seifert, P., Tesche, M., and Wandinger, U.: Profiling of fine and coarse particle mass: case studies of Saharan dust and Eyjafjallajökull/Grimsvötn volcanic plumes, *Atmospheric Chemistry and Physics*, 12, 9399–9415, <https://doi.org/10.5194/acp-12-9399-2012>, 2012.
- Ansmann, A., Rittmeister, F., Engelmann, R., Basart, S., Jorba, O., Spyrou, C., Remy, S., Skupin, A., Baars, H., Seifert, P., Senf, F., and Kanitz, T.: Profiling of Saharan dust from the Caribbean to western Africa – Part 2: Shipborne lidar measurements versus forecasts,  
695 *Atmospheric Chemistry and Physics*, 17, 14 987–15 006, <https://doi.org/10.5194/acp-17-14987-2017>, 2017.
- Ansmann, A., Mamouri, R.-E., Bühl, J., Seifert, P., Engelmann, R., Hofer, J., Nisantzi, A., Atkinson, J. D., Kanji, Z. A., Sierau, B., Vrekoussis, M., and Sciare, J.: Ice-nucleating particle versus ice crystal number concentration in altocumulus and cirrus layers embedded in Saharan dust: a closure study, *Atmospheric Chemistry and Physics*, 19, 15 087–15 115, <https://doi.org/10.5194/acp-19-15087-2019>, 2019a.
- 700 Ansmann, A., Mamouri, R.-E., Hofer, J., Baars, H., Althausen, D., and Abdullaev, S. F.: Dust mass, cloud condensation nuclei, and ice-nucleating particle profiling with polarization lidar: updated POLIPHON conversion factors from global AERONET analysis, *Atmospheric Measurement Techniques*, 12, 4849–4865, <https://doi.org/10.5194/amt-12-4849-2019>, 2019b.
- Ansmann, A., Ohneiser, K., Mamouri, R.-E., Knopf, D. A., Veselovskii, I., Baars, H., Engelmann, R., Foth, A., Jimenez, C., Seifert, P., and Barja, B.: Tropospheric and stratospheric wildfire smoke profiling with lidar: mass, surface area, CCN, and INP retrieval, *Atmospheric  
705 Chemistry and Physics*, 21, <https://doi.org/10.5194/acp-21-9779-2021>, 2021.
- Ansmann, A., Ohneiser, K., Engelmann, R., Radenz, M., Griesche, H., Hofer, J., Althausen, D., Creamean, J. M., Boyer, M. C., Knopf, D. A., Dahlke, S., Maturilli, M., Gebauer, H., Bühl, J., Jimenez, C., Seifert, P., and Wandinger, U.: Annual cycle of aerosol properties over the central Arctic during MOSAiC 2019–2020 – light-extinction, CCN, and INP levels from the boundary layer to the tropopause, *Atmospheric Chemistry and Physics*, 23, 12 821–12 849, <https://doi.org/10.5194/acp-23-12821-2023>, 2023.



- 710 Ansmann, A., Jimenez, C., Knopf, D. A., Roschke, J., Bühl, J., Ohneiser, K., and Engelmann, R.: Impact of wildfire smoke on Arctic cirrus formation – Part 2: Simulation of MOSAiC 2019–2020 cases, *Atmospheric Chemistry and Physics*, 25, 4867–4884, <https://doi.org/10.5194/acp-25-4867-2025>, 2025a.
- Ansmann, A., Jimenez, C., Roschke, J., Bühl, J., Ohneiser, K., Engelmann, R., Radenz, M., Griesche, H., Hofer, J., Althausen, D., Knopf, D. A., Dahlke, S., Gaudek, T., Seifert, P., and Wandinger, U.: Impact of wildfire smoke on Arctic cirrus formation – Part 1: Analysis of MOSAiC 2019–2020 observations, *Atmospheric Chemistry and Physics*, 25, 4847–4866, <https://doi.org/10.5194/acp-25-4847-2025>, 2025b.
- 715 Baars, H., Ansmann, A., Ohneiser, K., Haarig, M., Engelmann, R., Althausen, D., Hanssen, I., Gausa, M., Pietruczuk, A., Szkop, A., Stachlewska, I. S., Wang, D., Reichardt, J., Skupin, A., Mattis, I., Trickl, T., Vogelmann, H., Navas-Guzmán, F., Haeffele, A., Acheson, K., Ruth, A. A., Tatarov, B., Müller, D., Hu, Q., Podvin, T., Goloub, P., Veselovskii, I., Pietras, C., Haeffelin, M., Fréville, P., Sicard, M., Comerón, A., Fernández García, A. J., Molero Menéndez, F., Córdoba-Jabonero, C., Guerrero-Rascado, J. L., Alados-Arboledas, L., Bortoli, D., Costa, M. J., Dionisi, D., Liberti, G. L., Wang, X., Sannino, A., Papagiannopoulos, N., Boselli, A., Mona, L., D’Amico, G., Romano, S., Perrone, M. R., Belegante, L., Nicolae, D., Grigorov, I., Gialitaki, A., Amiridis, V., Soupiona, O., Papayannis, A., Mamouri, R.-E., Nisantzi, A., Heese, B., Hofer, J., Schechner, Y. Y., Wandinger, U., and Pappalardo, G.: The unprecedented 2017–2018 stratospheric smoke event: decay phase and aerosol properties observed with the EARLINET, *Atmospheric Chemistry and Physics*, 19, 15 183–15 198, <https://doi.org/10.5194/acp-19-15183-2019>, 2019.
- 725 Baars, H., Radenz, M., Floutsis, A. A., Engelmann, R., Althausen, D., Heese, B., Ansmann, A., Flament, T., Dabas, A., Trajon, D., Reitebuch, O., Bley, S., and Wandinger, U.: Californian Wildfire Smoke Over Europe: A First Example of the Aerosol Observing Capabilities of Aeolus Compared to Ground-Based Lidar, *Geophysical Research Letters*, 48, e2020GL092 194, <https://doi.org/10.1029/2020GL092194>, 2021.
- 730 Bellini, A., Diémoz, H., Di Liberto, L., Gobbi, G. P., Bracci, A., Pasqualini, F., and Barnaba, F.: ALICENET – an Italian network of automated lidar ceilometers for four-dimensional aerosol monitoring: infrastructure, data processing, and applications, *Atmospheric Measurement Techniques*, 17, 6119–6144, <https://doi.org/10.5194/amt-17-6119-2024>, 2024.
- Boichu, M., Grandin, R., Blarel, L., Torres, B., Derimian, Y., Goloub, P., Brogniez, C., Chiapello, I., Dubovik, O., Mathurin, T., Pascal, N., Patou, M., and Riedi, J.: Growth and Global Persistence of Stratospheric Sulfate Aerosols From the 2022 Hunga Tonga–Hunga Ha’apai Volcanic Eruption, *Journal of Geophysical Research: Atmospheres*, 128, e2023JD039 010, <https://doi.org/10.1029/2023JD039010>, 2023.
- 735 Cazorla, A., Casquero-Vera, J. A., Román, R., Guerrero-Rascado, J. L., Toledano, C., Cachorro, V. E., Orza, J. A. G., Cancillo, M. L., Serrano, A., Titos, G., Pandolfi, M., Alastuey, A., Hanrieder, N., and Alados-Arboledas, L.: Near-real-time processing of a ceilometer network assisted with sun-photometer data: monitoring a dust outbreak over the Iberian Peninsula, *Atmospheric Chemistry and Physics*, 17, 11 861–11 876, <https://doi.org/10.5194/acp-17-11861-2017>, 2017.
- 740 Choudhury, G. and Tesche, M.: Estimating cloud condensation nuclei concentrations from CALIPSO lidar measurements, *Atmospheric Measurement Techniques*, 15, 639–654, <https://doi.org/10.5194/amt-15-639-2022>, 2022.
- Choudhury, G., Ansmann, A., and Tesche, M.: Evaluation of aerosol number concentrations from CALIPSO with ATom airborne in situ measurements, *Atmospheric Chemistry and Physics*, 22, 7143–7161, <https://doi.org/10.5194/acp-22-7143-2022>, 2022.
- 745 Córdoba-Jabonero, C., Sicard, M., Ansmann, A., del Águila, A., and Baars, H.: Separation of the optical and mass features of particle components in different aerosol mixtures by using POLIPHON retrievals in synergy with continuous polarized Micro-Pulse Lidar (P-MPL) measurements, *Atmospheric Measurement Techniques*, 11, 4775–4795, <https://doi.org/10.5194/amt-11-4775-2018>, 2018.



- Dai, G., Wu, S., Long, W., Liu, J., Xie, Y., Sun, K., Meng, F., Song, X., Huang, Z., and Chen, W.: Aerosol and cloud data processing and optical property retrieval algorithms for the spaceborne ACDL/DQ-1, *Atmospheric Measurement Techniques*, 17, 1879–1890, <https://doi.org/10.5194/amt-17-1879-2024>, 2024.
- 750 DeMott, P. J., Prenni, A. J., Liu, X., Kreidenweis, S. M., Petters, M. D., Twohy, C. H., Richardson, M. S., Eidhammer, T., and Rogers, D. C.: Predicting global atmospheric ice nuclei distributions and their impacts on climate, *Proceedings of the National Academy of Sciences of the United States of America*, 107, 11 217–11 222, <https://doi.org/10.1073/pnas.0910818107>, 2010.
- DeMott, P. J., Prenni, A. J., McMeeking, G. R., Sullivan, R. C., Petters, M. D., Tobo, Y., Niemand, M., Möhler, O., Snider, J. R., Wang, Z., and Kreidenweis, S. M.: Integrating laboratory and field data to quantify the immersion freezing ice nucleation activity of mineral dust particles, *Atmospheric Chemistry and Physics*, 15, 393–409, <https://doi.org/10.5194/acp-15-393-2015>, 2015.
- 755 Dubovik, O. and King, M. D.: A flexible inversion algorithm for retrieval of aerosol optical properties from Sun and sky radiance measurements, *Journal of Geophysical Research: Atmospheres*, 105, 20 673–20 696, <https://doi.org/10.1029/2000JD900282>, 2000.
- Dubovik, O., Smirnov, A., Holben, B. N., King, M. D., Kaufman, Y. J., Eck, T. F., and Slutsker, I.: Accuracy assessment of aerosol optical properties retrieval from AERONET sun and sky radiance measurements, *Journal of Geophysical Research: Atmospheres*, 105, 9791–9806, <https://doi.org/10.1029/2000JD900040>, 2000.
- 760 Dubovik, O., Holben, B. N., Eck, T. F., Smirnov, A., Kaufman, Y. J., King, M. D., Tanré, D., and Slutsker, I.: Variability of absorption and optical properties of key aerosol types observed in worldwide locations, *Journal of the Atmospheric Sciences*, 59, 590–608, [https://doi.org/10.1175/1520-0469\(2002\)059<0590:VOAAOP>2.0.CO;2](https://doi.org/10.1175/1520-0469(2002)059<0590:VOAAOP>2.0.CO;2), 2002.
- Dubovik, O., Sinyuk, A., Lapyonok, T., Holben, B. N., Mishchenko, M., Yang, P., Eck, T. F., Volten, H., Muñoz, O., Wehlmann, B., van der Zande, W. J., Leon, J.-F., Sorokin, M., and Slutsker, I.: Application of spheroid models to account for aerosol particle nonsphericity in remote sensing of desert dust, *Journal of Geophysical Research: Atmospheres*, 11, D11 208, <https://doi.org/10.1029/2005JD006619>, 2006.
- 765 Düsing, S., Wehner, B., Seifert, P., Ansmann, A., Baars, H., Ditas, F., Henning, S., Ma, N., Poulain, L., Siebert, H., Wiedensohler, A., and Macke, A.: Helicopter-borne observations of the continental background aerosol in combination with remote sensing and ground-based measurements, *Atmospheric Chemistry and Physics*, 18, 1263–1290, <https://doi.org/10.5194/acp-18-1263-2018>, 2018.
- Engelmann, R., Ansmann, A., Ohneiser, K., Griesche, H., Radenz, M., Hofer, J., Althausen, D., Dahlke, S., Maturilli, M., Veselovskii, I., Jimenez, C., Wiesen, R., Baars, H., Bühl, J., Gebauer, H., Haarig, M., Seifert, P., Wandinger, U., and Macke, A.: Wildfire smoke, Arctic haze, and aerosol effects on mixed-phase and cirrus clouds over the North Pole region during MOSAiC: an introduction, *Atmospheric Chemistry and Physics*, 21, 13 397–13 423, <https://doi.org/10.5194/acp-21-13397-2021>, 2021.
- 775 Filioglou, M., Tiitta, P., Shang, X., Leskinen, A., Ahola, P., Pätsi, S., Saarto, A., Vakkari, V., Isopahkala, U., and Komppula, M.: Lidar estimates of birch pollen number, mass, and CCN-related concentrations, *Atmospheric Chemistry and Physics*, 25, 1639–1657, <https://doi.org/10.5194/acp-25-1639-2025>, 2025.
- Flentje, H., Mattis, I., Kipling, Z., Rémy, S., and Thomas, W.: Evaluation of ECMWF IFS-AER (CAMS) operational forecasts during cycle 41r1–46r1 with calibrated ceilometer profiles over Germany, *Geoscientific Model Development*, 14, 1721–1751, <https://doi.org/10.5194/gmd-14-1721-2021>, 2021.
- 780 Floutsi, A. A., Baars, H., Engelmann, R., Althausen, D., Ansmann, A., Bohlmann, S., Heese, B., Hofer, J., Kanitz, T., Haarig, M., Ohneiser, K., Radenz, M., Seifert, P., Skupin, A., Yin, Z., Abdullaev, S. F., Komppula, M., Filioglou, M., Giannakaki, E., Stachlewska, I. S., Janicka, L., Bortoli, D., Marinou, E., Amiridis, V., Gialitaki, A., Mamouri, R.-E., Barja, B., and Wandinger, U.: DeLiAn – a growing collection



- of depolarization ratio, lidar ratio and Ångström exponent for different aerosol types and mixtures from ground-based lidar observations,  
785 Atmospheric Measurement Techniques, 16, 2353–2379, <https://doi.org/10.5194/amt-16-2353-2023>, 2023.
- Floutsi, A. A., Baars, H., and Wandinger, U.: HETEAC-Flex: an optimal estimation method for aerosol typing based on lidar-derived intensive  
optical properties, Atmospheric Measurement Techniques, 17, 693–714, <https://doi.org/10.5194/amt-17-693-2024>, 2024.
- Froyd, K. D., Yu, P., chill, G. P., Brock, C. A., Kupc, A., Williamson, C. J., Jensen, E. J., Ray, E., Rosenlof, K. H., Bian, H., Darmenov, A. S.,  
Colarco, P. R., Diskin, G. S., Bui, T., and Murphy, D. M.: Dominant role of mineral dust in cirrus cloud formation revealed by global-scale  
790 measurements, Nature Geoscience, 15, 177–183, <https://doi.org/10.1038/s41561-022-00901-w>, 2022.
- Georgoulias, A. K., Marinou, E., Tsekeri, A., Proestakis, E., Akritidis, D., Alexandri, G., Zanis, P., Balis, D., Marengo, F., Tesche,  
M., and Amiridis, V.: A first case study of CCN concentrations from spaceborne lidar observations, Remote Sensing, 12,  
<https://doi.org/10.3390/rs12101557>, 2020.
- Gerasopoulos, E., Koulouri, E., Kalivitis, N., Kouvarakis, G., Saarikoski, S., Mäkelä, T., Hillamo, R., and Mihalopoulos, N.: Size-  
795 segregated mass distributions of aerosols over Eastern Mediterranean: seasonal variability and comparison with AERONET columnar  
size-distributions, Atmospheric Chemistry and Physics, 7, 2551–2561, <https://doi.org/10.5194/acp-7-2551-2007>, 2007.
- Giannakaki, E., Kokkalis, P., Marinou, E., Bartsotas, N. S., Amiridis, V., Ansmann, A., and Komppula, M.: The potential of elastic and  
polarization lidars to retrieve extinction profiles, Atmospheric Measurement Techniques, 13, 893–905, <https://doi.org/10.5194/amt-13-893-2020>, 2020.
- 800 Groß, S., Esselborn, M., Weinzierl, B., Wirth, M., Fix, A., and Petzold, A.: Aerosol classification by airborne high spectral resolution lidar  
observations, Atmospheric Chemistry and Physics, 13, 2487–2505, <https://doi.org/10.5194/acp-13-2487-2013>, 2013.
- Haarig, M., Ansmann, A., Gasteiger, J., Kandler, K., Althausen, D., Baars, H., Radenz, M., and Farrell, D. A.: Dry versus wet marine particle  
optical properties: RH dependence of depolarization ratio, backscatter, and extinction from multiwavelength lidar measurements during  
SALTRACE, Atmospheric Chemistry and Physics, 17, 14 199–14 217, <https://doi.org/10.5194/acp-17-14199-2017>, 2017.
- 805 Haarig, M., Ansmann, A., Baars, H., Jimenez, C., Veselovskii, I., Engelmann, R., and Althausen, D.: Depolarization and lidar ratios at 355,  
532, and 1064 nm and microphysical properties of aged tropospheric and stratospheric Canadian wildfire smoke, Atmospheric Chemistry  
and Physics, 18, 11 847–11 861, <https://doi.org/10.5194/acp-18-11847-2018>, 2018.
- Haarig, M., Walser, A., Ansmann, A., Dollner, M., Althausen, D., Sauer, D., Farrell, D., and Weinzierl, B.: Profiles of cloud condensation  
nuclei, dust mass concentration, and ice-nucleating-particle-relevant aerosol properties in the Saharan Air Layer over Barbados from  
810 polarization lidar and airborne in situ measurements, Atmospheric Chemistry and Physics, 19, 13 773–13 788, <https://doi.org/10.5194/acp-19-13773-2019>, 2019.
- Haarig, M., Ansmann, A., Engelmann, R., Baars, H., Toledano, C., Torres, B., Althausen, D., Radenz, M., and Wandinger, U.: First triple-  
wavelength lidar observations of depolarization and extinction-to-backscatter ratios of Saharan dust, Atmospheric Chemistry and Physics,  
22, 355–369, <https://doi.org/10.5194/acp-22-355-2022>, 2022.
- 815 Haarig, M., Baars, H., König, L., Donovan, D., Ansmann, A., Gast, B., Floutsi, A. A., Hogan, R. J., Chantry, A., Marnas, F., van Zadelhoff,  
G.-J., and Wandinger, U.: The life cycle of a stratospheric smoke plume as seen from EarthCARE - tracking a plume from Canada to  
Europe, ESS Open Archive [preprint], <https://doi.org/10.22541/essoar.176114361.17960897/v1>, 2025a.
- Haarig, M., Engelmann, R., Baars, H., Gast, B., Althausen, D., and Ansmann, A.: Discussion of the spectral slope of the lidar ra-  
tio between 355 and 1064 nm from multiwavelength Raman lidar observations, Atmospheric Chemistry and Physics, 25, 7741–7763,  
820 <https://doi.org/10.5194/acp-25-7741-2025>, 2025b.



- Hänel, G.: The Properties of Atmospheric Aerosol Particles as Functions of the Relative Humidity at Thermodynamic Equilibrium with the Surrounding Moist Air, vol. 19 of *Advances in Geophysics*, pp. 73–188, Elsevier, [https://doi.org/10.1016/S0065-2687\(08\)60142-9](https://doi.org/10.1016/S0065-2687(08)60142-9), 1976.
- He, Y., Yin, Z., Ansmann, A., Liu, F., Wang, L., Jing, D., and Shen, H.: POLIPHON conversion factors for retrieving dust-related cloud condensation nuclei and ice-nucleating particle concentration profiles at oceanic sites, *Atmospheric Measurement Techniques*, 16, 1951–1970, <https://doi.org/10.5194/amt-16-1951-2023>, 2023.
- 825 He, Y., Choudhury, G., Tesche, M., Ansmann, A., Yi, F., Müller, D., and Yin, Z.: Extended POLIPHON dust conversion factor dataset for lidar-derived cloud condensation nuclei and ice-nucleating particle concentration profiles, *Atmospheric Measurement Techniques*, 18, 5669–5685, <https://doi.org/10.5194/amt-18-5669-2025>, 2025a.
- He, Y., Seifert, P., Jimenez, C., Radenz, M., Ansmann, A., Bühl, J., Mamouri, R.-E., and Barja González, B.: Response of Mixed-Phase Cloud Microphysics to Aerosol Perturbations at the Contrasting Sites of Limassol, Cyprus, and Punta Arenas, Chile, *Journal of Geophysical Research: Atmospheres*, 130, e2024JD043 157, <https://doi.org/doi.org/10.1029/2024JD043157>, 2025b.
- 830 Hofer, J., Ansmann, A., Althausen, D., Engelmann, R., Baars, H., Abdullaev, S. F., and Makhmudov, A. N.: Long-term profiling of aerosol light extinction, particle mass, cloud condensation nuclei, and ice-nucleating particle concentration over Dushanbe, Tajikistan, in *Central Asia*, *Atmospheric Chemistry and Physics*, 20, 4695–4711, <https://doi.org/10.5194/acp-20-4695-2020>, 2020.
- 835 Hofer, J., König, L., and Ansmann, A.: Updated POLIPHON conversion factors for lidar and ceilometer applications, Zenodo [dataset], 2026.
- Holben, B. N., Eck, T. F., Slutsker, I., Tanré, D., Buis, J. P., Setzer, A., Vermote, E., Reagan, J. A., Kaufman, Y. J., Nakajima, T., Lavenu, F., Jankowiak, I., and Smirnov, A.: AERONET - A federated instrument network and data archive for aerosol characterization, *Remote Sensing of Environment*, 66, 1–16, [https://doi.org/10.1016/S0034-4257\(98\)00031-5](https://doi.org/10.1016/S0034-4257(98)00031-5), 1998.
- Jäger, H. and Deshler, T.: Lidar backscatter to extinction, mass and area conversions for stratospheric aerosols based on midlatitude balloonborne size distribution measurements, *Geophysical Research Letters*, 29, 1929, <https://doi.org/10.1029/2002GL015609>, 2002.
- 840 Jäger, H. and Deshler, T.: Correction to "Lidar backscatter to extinction, mass and area conversions for stratospheric aerosols based on midlatitude balloonborne size distribution measurements", *Geophysical Research Letters*, 30, 1382, <https://doi.org/10.1029/2003GL017189>, 2003.
- Janicka, L., Davulienė, L., Bycenkienė, S., and Stachlewska, I. S.: Long term observations of biomass burning aerosol over Warsaw by means of multiwavelength lidar, *Optics Express*, 31, 33 150–33 174, <https://doi.org/10.1364/OE.496794>, 2023.
- 845 Jimenez, C., Ansmann, A., Engelmann, R., Donovan, D., Malinka, A., Seifert, P., Wiesen, R., Radenz, M., Yin, Z., Bühl, J., Schmidt, J., Barja, B., and Wandinger, U.: The dual-field-of-view polarization lidar technique: a new concept in monitoring aerosol effects in liquid-water clouds – case studies, *Atmospheric Chemistry and Physics*, 20, 15 265–15 284, <https://doi.org/10.5194/acp-20-15265-2020>, 2020.
- Jimenez, C., Ansmann, A., Ohneiser, K., Griesche, H., Engelmann, R., Radenz, M., Hofer, J., Althausen, D., Knopf, D. A., Dahlke, S., Bühl, J., Baars, H., Seifert, P., and Wandinger, U.: MOSAiC studies of long-lasting mixed-phase cloud events and analysis of the liquid-phase properties of Arctic clouds, *Atmospheric Chemistry and Physics*, 25, 12 955–12 981, <https://doi.org/10.5194/acp-25-12955-2025>, 2025.
- 850 Kanji, Z. A., Ladino, L. A., Wex, H., Boose, Y., Burkert-Kohn, M., and Cziczo, D. J. and Krämer, M.: Overview of ice nucleating particles, *Meteorological Monographs*, 58, 1.1–1.33, <https://doi.org/10.1175/AMSMONOGRAPHS-D-16-0006.1>, 2017.
- Knopf, D. A. and Alpert, P. A.: A water activity based model of heterogeneous ice nucleation kinetics for freezing of water and aqueous solution droplets, *Faraday Discussions*, 165, 513–534, <https://doi.org/10.1039/c3fd00035d>, 2013.
- 855 Knopf, D. A., Silber, I., Riemer, N., Fridlind, A. M., and Ackerman, A. S.: A 1D Model for Nucleation of Ice From Aerosol Particles: An Application to a Mixed-Phase Arctic Stratus Cloud Layer, *Journal of Advances in Modeling Earth Systems*, 15, e2023MS003 663, <https://doi.org/10.1029/2023MS003663>, 2023.



- 860 Koehler, K. A., Kreidenweis, S. M., DeMott, P. J., Petters, M-D. and Prenni, A. J., and Carrico, C. M.: Hygroscopicity and cloud droplet activation of mineral dust aerosol, *Geophysical Research Letters*, 36, L08 805, <https://doi.org/10.1029/2009GL037348>, 2009.
- Koop, T., Luo, B. P., Tsias, A., and Peter, T.: Water activity as the determinant for homogeneous ice nucleation in aqueous solutions, *Nature*, 406, 611–61, <https://doi.org/10.1038/35020537>, 2000.
- 865 Kulkarni, G., Mei, F., Sivaraman, C., Wang, J., Shilling, J. E., Newsom, R. K., Christensen, M. W., Berg, L. K., and Fast, J. D.: Assessment of Extinction-, Satellite-, and Model-Based Vertical Cloud Condensation Nuclei (CCN) Retrieval Methods Using Airborne CCN Measurements Over the Southern Great Plains, *Journal of Geophysical Research: Atmospheres*, 130, e2024JD042565, <https://doi.org/10.1029/2024JD042565>, 2025.
- Kumar, P., Sokolik, I. N., and Nenes, A.: Parameterization of cloud droplet formation for global and regional models: including adsorption activation from insoluble CCN, *Atmospheric Chemistry and Physics*, 9, 2517–2532, <https://doi.org/10.5194/acp-9-2517-2009>, 2009.
- 870 Lenhardt, E. D., Gao, L., Redemann, J., Xu, F., Burton, S. P., Cairns, B., Chang, I., Ferrare, R. A., Hostetler, C. A., Saide, P. E., Howes, C., Shinozuka, Y., Stamnes, S., Kacarab, M., Dobracki, A., Wong, J., Freitag, S., and Nenes, A.: Use of lidar aerosol extinction and backscatter coefficients to estimate cloud condensation nuclei (CCN) concentrations in the southeast Atlantic, *Atmospheric Measurement Techniques*, 16, 2037–2054, <https://doi.org/10.5194/amt-16-2037-2023>, 2023.
- Malollari, G., Ansmann, A., Chudnovsky, A., Baars, H., Engelmann, R., Althausen, D., Heese, B., and Shallari, S.: Vertical profiling of residential wood combustion aerosols over Tirana, Albania: First lidar-based observations, *Atmospheric Environment*, 359, 121 358, <https://doi.org/10.1016/j.atmosenv.2025.121358>, 2025.
- 875 Mamali, D., Marinou, E., Sciare, J., Pikridas, M., Kokkalis, P., Kottas, M., Biniotoglou, I., Tsekeri, A., Keleshis, C., Engelmann, R., Baars, H., Ansmann, A., Amiridis, V., Russchenberg, H., and Biskos, G.: Vertical profiles of aerosol mass concentration derived by unmanned airborne in situ and remote sensing instruments during dust events, *Atmospheric Measurement Techniques*, 11, 2897–2910, <https://doi.org/10.5194/amt-11-2897-2018>, 2018.
- 880 Mamouri, R. E. and Ansmann, A.: Fine and coarse dust separation with polarization lidar, *Atmospheric Measurement Techniques*, 7, 3717–3735, <https://doi.org/10.5194/amt-7-3717-2014>, 2014.
- Mamouri, R.-E. and Ansmann, A.: Potential of polarization lidar to provide profiles of CCN- and INP-relevant aerosol parameters, *Atmospheric Chemistry and Physics*, 16, 5905–5931, <https://doi.org/10.5194/acp-16-5905-2016>, 2016.
- Mamouri, R.-E. and Ansmann, A.: Potential of polarization/Raman lidar to separate fine dust, coarse dust, maritime, and anthropogenic aerosol profiles, *Atmospheric Measurement Techniques*, 10, 3403–3427, <https://doi.org/10.5194/amt-10-3403-2017>, 2017.
- 885 Mamouri, R.-E., Ansmann, A., Ohneiser, K., Knopf, D. A., Nisantzi, A., Bühl, J., Engelmann, R., Skupin, A., Seifert, P., Baars, H., Ene, D., Wandinger, U., and Hadjimitsis, D.: Wildfire smoke triggers cirrus formation: lidar observations over the eastern Mediterranean, *Atmospheric Chemistry and Physics*, 23, 14 097–14 114, <https://doi.org/10.5194/acp-23-14097-2023>, 2023.
- Marinou, E., Tesche, M., Nenes, A., Ansmann, A., Schrod, J., Mamali, D., Tsekeri, A., Pikridas, M., Baars, H., Engelmann, R., Voudouri, K.-A., Solomos, S., Sciare, J., Groß, S., Ewald, F., and Amiridis, V.: Retrieval of ice-nucleating particle concentrations from lidar observations and comparison with UAV in situ measurements, *Atmospheric Chemistry and Physics*, 19, 11 315–11 342, <https://doi.org/10.5194/acp-19-11315-2019>, 2019.
- 890 McCluskey, C. S., Ovadnevaite, J., Rinaldi, M., Atkinson, J., Belosi, F., Ceburnis, D., Marullo, S., Hill, T. C. J., Lohmann, U., Kanji, Z. A., O’Dowd, C., Kreidenweis, S. M., and DeMott, P. J.: Marine and terrestrial organic ice-nucleating particles in pristine marine to continentally influenced Northeast Atlantic air masses, *Journal of Geophysical Research: Atmospheres*, 123, 6196–6212, <https://doi.org/10.1029/2017JD028033>, 2018.



- Müller, D., Ansmann, A., Mattis, I., Tesche, M., Wandinger, U., Althausen, D., and Pisani, G.: Aerosol-type-dependent lidar ratios observed with Raman lidar, *Journal of Geophysical Research: Atmospheres*, 112, D16 202, <https://doi.org/10.1029/2006JD008292>, 2007.
- 900 Omar, A. H., Won, J.-G., Winker, D. M., Yoon, S.-C., Dubovik, O., and McCormick, M. P.: Development of global aerosol models using cluster analysis of Aerosol Robotic Network (AERONET) measurements, *Journal of Geophysical Research: Atmospheres*, 110, <https://doi.org/10.1029/2004JD004874>, 2005.
- Omar, A. H., Winker, D. M., Vaughan, M. A., Hu, Y., Trepte, C. R., Ferrare, R. A., Lee, K.-P., Hostetler, C. A., Kittaka, C., Rogers, R. R., Kuehn, R. E., and Liu, Z.: The CALIPSO Automated Aerosol Classification and Lidar Ratio Selection Algorithm, *Journal of Atmospheric and Oceanic Technology*, 26, 1994 – 2014, <https://doi.org/10.1175/2009JTECHA1231.1>, 2009.
- 905 Pappalardo, G., Amodeo, A., Apituley, A., Comeron, A., Freudenthaler, V., Linné, H., Ansmann, A., Bösenberg, J., D'Amico, G., Mattis, I., Mona, L., Wandinger, U., Amiridis, V., Alados-Arboledas, L., Nicolae, D., and Wiegner, M.: EARLINET: towards an advanced sustainable European aerosol lidar network, *Atmospheric Measurement Techniques*, 7, 2389–2409, <https://doi.org/10.5194/amt-7-2389-2014>, 2014.
- Proestakis, E., Amiridis, V., García-Pando, C. P., Tsyro, S., Griesfeller, J., Gkikas, A., Georgiou, T., Ageitos, M. G., Escribano, J., Myriokefalitakis, S., Masso, E. B., Di Tomaso, E., Basart, S., Stuut, J.-B. W., and Benedetti, A.: Quantifying dust deposition over the Atlantic Ocean, *Earth System Science Data*, 17, 4351–4395, <https://doi.org/10.5194/essd-17-4351-2025>, 2025a.
- 910 Proestakis, E., Papachristopoulou, K., Georgiou, T., Chatoutsidou, S. E., Lazaridis, M., Gkikas, A., Fountoulakis, I., Tsikoudi, I., Petrakis, M. P., and Amiridis, V.: Atmospheric dust and air quality over large-cities and megacities of the world, *Atmospheric Chemistry and Physics*, 25, 14 777–14 823, <https://doi.org/10.5194/acp-25-14777-2025>, 2025b.
- Pruppacher, H. R. and Klett, J. D.: *Microphysics of clouds and precipitation*, Springer Dordrecht, <https://doi.org/10.1007/978-0-306-48100-0>, 1997.
- 915 Radenz, M., Bühl, J., Seifert, P., Baars, H., Engelmann, R., Barja González, B., Mamouri, R.-E., Zamorano, F., and Ansmann, A.: Hemispheric contrasts in ice formation in stratiform mixed-phase clouds: disentangling the role of aerosol and dynamics with ground-based remote sensing, *Atmospheric Chemistry and Physics*, 21, 17 969–17 994, <https://doi.org/10.5194/acp-21-17969-2021>, 2021a.
- Radenz, M., Seifert, P., Baars, H., Floutsi, A. A., Yin, Z., and Bühl, J.: Automated time–height-resolved air mass source attribution for profiling remote sensing applications, *Atmospheric Chemistry and Physics*, 21, 3015–3033, <https://doi.org/10.5194/acp-21-3015-2021>, 2021b.
- 920 Radenz, M., Engelmann, R., Henning, S., Schmithüsen, H., Baars, H., Frey, M. M., Weller, R., Bühl, J., Jimenez, C., Roschke, J., Muser, L. O., Wullenweber, N., Zeppenfeld, S., Griesche, H., Wandinger, U., and Seifert, P.: Ground-Based Remote Sensing of Aerosol, Clouds, Dynamics, and Precipitation in Antarctica: First Results from the 1-Year COALA Campaign at Neumayer Station III in 2023, *Bulletin of the American Meteorological Society*, 105, E1438 – E1457, <https://doi.org/10.1175/BAMS-D-22-0285.1>, 2024.
- 925 Rogozovsky, I., Ansmann, A., Hofer, J., and Chudnovsky, A.: Unveiling Atmospheric Layers: Vertical Pollution Patterns and Prospects for High-Resolution Aerosol Retrievals Using the Eastern Mediterranean as a Case Study, *Environmental Science & Technology*, 59, 12 181–12 195, <https://doi.org/10.1021/acs.est.4c14556>, 2025.
- Schneider, L., Schrod, J., Weber, D., Bingemer, H., Kandler, K., Curtius, J., and Ebert, M.: Analyzing the chemical composition, morphology, and size of ice-nucleating particles by coupling a scanning electron microscope to an offline diffusion chamber, *Atmospheric Measurement Techniques*, 18, 5223–5245, <https://doi.org/10.5194/amt-18-5223-2025>, 2025.
- 930 Seifert, A., Bachmann, V., Filipitsch, F., Förstner, J., Grams, C. M., Hoshyaripour, G. A., Quinting, J., Rohde, A., Vogel, H., Wagner, A., and Vogel, B.: Aerosol–cloud–radiation interaction during Saharan dust episodes: the dusty cirrus puzzle, *Atmospheric Chemistry and Physics*, 23, 6409–6430, <https://doi.org/10.5194/acp-23-6409-2023>, 2023.



- 935 Shang, X., Lipponen, A., Filioglou, M., Sundström, A.-M., Parrington, M., Buchard, V., Darmenov, A. S., Welton, E. J., Marinou, E., Amiridis, V., Sicard, M., Rodríguez-Gómez, A., Komppula, M., and Mielonen, T.: Monitoring biomass burning aerosol transport using CALIOP observations and reanalysis models: a Canadian wildfire event in 2019, *Atmospheric Chemistry and Physics*, 24, 1329–1344, <https://doi.org/10.5194/acp-24-1329-2024>, 2024.
- Shen, H., Yin, Z., He, Y., Ansmann, A., Zhan, Y., Wang, L., and Jing, D.: Impact of Asian dust on cirrus formation over the central Pacific: CALIOP- and Cloud-Sat observation-based case studies, *Journal of Geophysical Research: Atmospheres*, 129, e2024JD041265, <https://doi.org/10.1029/2024JD041265>, 2024.
- 940 Shinozuka, Y., Clarke, A. D., Nenes, A., Jefferson, A., Wood, R., McNaughton, C. S., Ström, J., Tunved, P., Redemann, J., Thornhill, K. L., Moore, R. H., Latham, T. L., Lin, J. J., and Yoon, Y. J.: The relationship between cloud condensation nuclei (CCN) concentration and light extinction of dried particles: indications of underlying aerosol processes and implications for satellite-based CCN estimates, *Atmospheric Chemistry and Physics*, 15, 7585–7604, <https://doi.org/10.5194/acp-15-7585-2015>, 2015.
- 945 Skupin, A., Ansmann, A., Engelmann, R., Seifert, P., and Müller, T.: Four-year long-path monitoring of ambient aerosol extinction at a central European urban site: dependence on relative humidity, *Atmospheric Chemistry and Physics*, 16, 1863–1876, <https://doi.org/10.5194/acp-16-1863-2016>, 2016.
- Stein, A. F., Draxler, R. R., Rolph, G. D., Stunder, B. J. B., Cohen, M. D., and Ngan, F.: NOAA’s HYSPLIT Atmospheric Transport and Dispersion Modeling System, *Bulletin of the American Meteorological Society*, 96, 2059–2077, <https://doi.org/10.1175/BAMS-D-14-00110.1>, 2015.
- 950 Tesche, M., Ansmann, A., Müller, D., Althausen, D., Engelmann, R., Freudenthaler, V., and Groß, S.: Vertically resolved separation of dust and smoke over Cape Verde using multiwavelength Raman and polarization lidars during Saharan Mineral Dust Experiment 2008, *Journal of Geophysical Research: Atmospheres*, 114, D13 202, <https://doi.org/10.1029/2009JD011862>, 2009.
- 955 Tobo, Y., Prenni, A. J., DeMott, P. J., Huffman, J. A., McCluskey, C. S., Tian, G., Pöhlker, C., Pöschl, U., and Kreidenweis, S. M.: Biological aerosol particles as a key determinant of ice nuclei populations in a forest ecosystem, *Journal of Geophysical Research: Atmospheres*, 118, 10,100–10,110, <https://doi.org/10.1002/jgrd.50801>, 2013.
- Tobo, Y., DeMott, P. J., Hill, T. C. J., Prenni, A. J., Swoboda-Colberg, N. G., Franc, G. D., and Kreidenweis, S. M.: Organic matter matters for ice nuclei of agricultural soil origin, *Atmospheric Chemistry and Physics*, 14, 8521–8531, <https://doi.org/10.5194/acp-14-8521-2014>, 2014.
- 960 Trapon, D., Baars, H., Floutsi, A. A., Bley, S., Haarrig, M., Lacour, A., Flament, T., Dabas, A., Nehrir, A. R., Ehlers, F., and Huber, D.: Cross-validations of the Aeolus aerosol products and new developments with airborne high-spectral-resolution lidar measurements above the tropical Atlantic during JATAC, *Atmospheric Measurement Techniques*, 18, 3873–3896, <https://doi.org/10.5194/amt-18-3873-2025>, 2025.
- 965 Ullrich, R., Hoose, C., Möhler, O., Niemand, M., Wagner, R., Höhler, K., Hiranuma, N., Saathoff, H., and Leisner, T.: A New Ice Nucleation Active Site Parameterization for Desert Dust and Soot, *Journal of the Atmospheric Sciences*, 74, 699–717, <https://doi.org/10.1175/JAS-D-16-0074.1>, 2017.
- Veselovskii, I., Hu, Q., Goloub, P., Podvin, T., Dubois, G., Kolgotin, A., and Korenskii, M.: Impact of water uptake on fluorescence of atmospheric aerosols: insights from Mie–Raman–fluorescence lidar measurements, *Atmospheric Measurement Techniques*, 18, 6039–6051, <https://doi.org/10.5194/amt-18-6039-2025>, 2025.
- 970



- Wandinger, U., Ansmann, A., Reichardt, J., and Deshler, T.: Determination of stratospheric aerosol microphysical properties from independent extinction and backscattering measurements with a Raman lidar, *Applied Optics*, 34, 8315, <https://doi.org/10.1364/AO.34.008315>, 1995.
- 975 Wandinger, U., Floutsis, A. A., Baars, H., Haarrig, M., Ansmann, A., Hünerbein, A., Docter, N., Donovan, D., van Zadelhoff, G.-J., Mason, S., and Cole, J.: HETEAC – the Hybrid End-To-End Aerosol Classification model for EarthCARE, *Atmospheric Measurement Techniques*, 16, 2485–2510, <https://doi.org/10.5194/amt-16-2485-2023>, 2023.
- Wang, B., Lambe, A. T., Massoli, P., Onasch, T. B., Davidovits, P., Worsnop, D. R., and Knopf, D. A.: The deposition ice nucleation and immersion freezing potential of amorphous secondary organic aerosol: Pathways for ice and mixed-phase cloud formation, *Journal of Geophysical Research: Atmospheres*, 117, D16 209, <https://doi.org/https://doi.org/10.1029/2012JD018063>, 2012.
- 980 Wehr, T., Kubota, T., Tzeremes, G., Wallace, K., Nakatsuka, H., Ohno, Y., Koopman, R., Rusli, S., Kikuchi, M., Eisinger, M., Tanaka, T., Taga, M., Deghaye, P., Tomita, E., and Bernaerts, D.: The EarthCARE mission – science and system overview, *Atmospheric Measurement Techniques*, 16, 3581–3608, <https://doi.org/10.5194/amt-16-3581-2023>, 2023.
- Wieder, J., Ihn, N., Mignani, C., Haarrig, M., Bühl, J., Seifert, P., Engelmann, R., Ramelli, F., Kanji, Z. A., Lohmann, U., and Henneberger, J.: Retrieving ice-nucleating particle concentration and ice multiplication factors using active remote sensing validated by in situ observations, *Atmospheric Chemistry and Physics*, 22, 9767–9797, <https://doi.org/10.5194/acp-22-9767-2022>, 2022.
- 985 Winker, D. M., Vaughan, M. A., Omar, A., Hu, Y., Powell, K. A., Liu, Z., Hunt, W. H., and Young, S. A.: Overview of the CALIPSO mission and CALIOP data processing algorithms, *Journal of Atmospheric and Oceanic Technology*, 26, 2310–2323, <https://doi.org/10.1175/2009JTECHA1281.1>, 2009.
- Winker, D. M., Pelon, J., Coakley, J. A., Ackerman, S. A., Charlson, R. J., Colarco, P. R., Flamant, P. H., Fu, Q., Hoff, R. M., Kittaka, C., 990 Kubar, T. L., Le Treut, H., McCormick, M. P., Mégie, G., Poole, L. R., Powell, K., Trepte, C. R., Vaughan, M. A., and Wielicki, B. A.: The CALIPSO mission: A global 3D view of aerosols and clouds, *Bulletin of the American Meteorological Society*, 91, 1211–1229, <https://doi.org/10.1175/2010BAMS3009.1>, 2010.
- York, D., Evensen, N. M., Martínez, M. L., and De Basabe Delgado, J.: Unified equations for the slope, intercept, and standard errors of the best straight line, *American Journal of Physics*, 72, 367–375, <https://doi.org/10.1119/1.1632486>, 2004.